

Detection and assignment of ozone bands near 95% of the dissociation threshold: Ultrasensitive experiments for probing potential energy function and vibrational dynamics

Semen Vasilchenko,^{1,3} Alain Barbe,² Evgeniya Starikova,^{1,3} Samir Kassi ,⁴ Didier Mondelain,⁴ Alain Campargue ,^{4,*} and Vladimir Tyuterev ^{3,2}

¹*V. E. Zuev Institute of Atmospheric Optics SB RAS, 1 Akademician Zuev square, 634055 Tomsk, Russia*

²*Groupe de Spectrométrie Moléculaire et Atmosphérique, UMR CNRS 7331, UFR Sciences Exactes et Naturelles, BP 1039-51687 Reims Cedex 2, France*

³*Laboratory of Quantum Mechanics of Molecules and Radiative Processes, Tomsk State University, 36 Lenin Avenue, 634050 Tomsk, Russia*

⁴*Université Grenoble Alpes, CNRS, LIPhy, 38000 Grenoble, France*

 (Received 18 June 2020; revised 7 September 2020; accepted 28 September 2020; published 6 November 2020)

Ozone formation and depletion play a key role in various physical and chemical atmospheric processes which remain to be understood in more detail. The modeling of such phenomena based on ozone dynamics calculations requires a detailed knowledge of quantum states, transition probabilities, and ozone potential energy surface (PES) near the dissociation threshold D_0 . Knowledge of highly excited rovibrational states with energies approaching D_0 is necessary for a reliable interpretation of satellite measurements of the ozone absorption or emission in the upper atmosphere in nonlocal thermodynamic equilibrium conditions. In addition, these states provide an ideal probe of PESs computed by *ab initio* methods but their detection by absorption spectroscopy is particularly challenging due to the sharp decrease of the intensity with the energy of the corresponding vibrational combination and overtone bands. In this work, two very high-energy vibrational bands are detected by high sensitivity cavity ring-down spectroscopy providing a noise equivalent absorption α_{\min} on the order of a few 10^{-11} cm^{-1} . The corresponding cold bands, assigned as $\nu_1 + 6\nu_2 + 3\nu_3$ and $6\nu_1 + \nu_2 + \nu_3$ centered at 7969 and 7993 cm^{-1} , respectively, are about nine orders of magnitude less intense than the well-known ν_3 fundamental band near 10 μm . The spectrum analysis allowed for the experimental determination of 240 rovibrational energy levels of the upper vibrational states. The corresponding rotational patterns, located between 93.1% and 96.7% of the dissociation threshold, are the most excited ones measured so far by absorption spectroscopy. The values of the band centers and rotational constants derived from the spectrum analysis provide further confirmation of the absence of an activation barrier on the minimum-energy path towards the dissociation threshold [Tyuterev *et al.*, *Phys. Rev. Lett.* **113**, 143002 (2014)]. The vibrational dynamics is discussed in the context of the radiative transition probabilities and related Einstein coefficients for the observed bands. Another important question in the context of the nuclear dynamics concerns the interaction among the three identical potential wells of the ozone molecule in the ground electronic state, which appears to be due to the Jahn-Teller effect. Recent theoretical results accounting for the three potential wells in a full symmetry approach predicted that vibration states should exhibit deviations from the conventional one-potential-well *ab initio* calculations, near the dissociation threshold. In the present work, we observe a better agreement of the experimentally determined energy value with the three-wells prediction for the (1,6,3) vibrational state involving a large simultaneous excitation of both bending ($\nu_2 = 6$) and asymmetric stretch ($\nu_3 = 3$) vibrations pointing towards a nearby well. This could be tentatively interpreted as a manifestation of the three-wells effect.

DOI: [10.1103/PhysRevA.102.052804](https://doi.org/10.1103/PhysRevA.102.052804)

I. INTRODUCTION

Various physical and chemical processes involved in the formation and depletion of ozone in the atmosphere have attracted attention over the years [1–13]. In this context, several aspects of the ozone dynamics remain to be understood for an accurate modeling at the molecular level. This concerns in particular, the knowledge of the highly excited quantum states and associated transition probabilities, near the dissociation threshold, D_0 , evaluated around 8560 cm^{-1}

(as cited in [14,15]) from thermochemical measurements by Ruscic *et al.* [16].

High-energy rovibrational states have a major importance in various fields including the possible tunneling between potential wells [17,18], nonadiabatic coupling with excited electronic states [19–22], isotopic exchange reactions [23–27], unusual properties related to isotopic anomalies of the ozone formation [11,28,29], which are not yet fully understood at the molecular level. In practical terms, they are necessary for a reliable interpretation of satellite measurements of the ozone absorption or emission in the upper atmosphere [30–32] in nonlocal thermodynamic equilibrium (non-LTE) conditions [33,34]. The characterization of these

*Alain.Campargue@univ-grenoble-alpes.fr

excited states is a challenging task both for experiment and theory because of the complicated electronic structure of this unstable molecule [14,15,19–22,35–40], with significant discrepancies among published theoretical predictions [15,18,36,39–41]. Many related aspects are expected to benefit from extended experimental information.

Available non-LTE theories [33,34,42] assume that about half of ozone molecules populate highly excited vibrational states in the upper atmosphere of the Earth during the stabilization stage of the ozone formation. The corresponding “nascent population” plays a key role in the non-LTE radiative transfer models [33,34,42], but reliable knowledge of the properties of these states (energies, transition probabilities) is very limited.

In laboratory conditions, an access to highly excited ozone states is known to be a true challenge. An excitation by collisions (heating) is hazardous due to the explosion risk, whereas direct photon excitation at room temperature requires extreme sensitivity of the experimental setup because the transition probabilities from the ground vibrational state to excited ones near D_0 fall down by nine or ten orders of magnitude with respect to fundamental or low overtone bands. As a result, experimental information for vibrational energies and the dynamics of the nuclear motion just below the dissociation threshold is at present mostly lacking.

This work aims at experimental probing quantum rovibrational states towards the dissociation threshold by cavity-ring-down spectroscopy (CRDS) with a routine noise equivalent absorption, α_{\min} , on the order of a few 10^{-11} cm^{-1} . As described in Secs. II and III, the achieved sensitivity allowed for extending previous CRDS measurements above 7920 cm^{-1} and for the detection of the most excited absorption vibrational bands of ozone reported so far. As a result, the highest rovibrational energy level determined from the analysis is only 3.3% below the dissociation threshold.

The analyses of the recorded bands (Sec. III) will certainly be important for validation tests of theoretical *ab initio* methods as available potential energy surfaces (PESs) provide quite different predictions [15,18,36,39–41] both for the shape of the surfaces and for vibrational states and their quantum assignments. For example, according to the pioneer full-dimensional *ab initio* calculations of Ref. [36], which have been widely used for dynamics studies during the last decades, our spectral range would fall in the continuum absorption above D_0 , whereas our measurements clearly show the existence of bound rovibrational states (Secs. II and III).

The challenges in accessing this spectral range go well beyond the construction of line lists of transitions. Among them, there are issues of general interest for fundamental molecular physics concerning the vibrational dynamics near the dissociation threshold and the trends of transition probabilities (linked to Einstein coefficients) while the difference in quantum numbers Δv increases. Several studies have attempted to derive a general “normal intensity distribution” (“rule of thumb”) [43,44] for the decreasing rate of band intensities, claiming that this rate could serve as a critical validation for the inner part of the potential function [44,45]. This was based on an implicit assumption that the absorption intensities for high-energy bands are dominated by stretching overtones with respect to the combination bands which

involve bending vibrations. The present observations provide instructive insights into the question of whether this is always true near the D_0 limit.

Other issues are specific to the particular case of ozone. Advanced dynamical experiments [46–48] have shown that a simple “statistical” approximation [5] of energy repartition in vibrational modes, which has been employed in many earlier models for anomalous effects in the ozone formation, is not valid [11]. This is a strong incentive for a detailed experimental study of individual bands, of the vibrational dynamics of high-energy states, and of their interactions.

Due to the Jahn-Teller effect [19,22,49], the ozone molecule possesses three identical C_{2v} potential wells in the ground electronic state separated by relatively high barriers among the equilibrium geometries [36]. This explains a somewhat surprising fact that a molecule with three identical atoms is experimentally seen as an asymmetric top [50–53] with three different rotational constants depending on vibrational excitation. A permutation of the oxygen atoms makes the ozone molecule “travels” from one well to another [17,18]. The interaction between these three wells plays a crucial role in isotopic exchange processes that exhibit anomalous properties [10,23–27].

On the theoretical side, Kokoouline *et al.* [18] have recently studied interactions among the three wells and their possible impacts on the vibrational band centers using the symmetrized *ab initio* PES of Ref. [15]. The full symmetry approach reported in [17,18] predicts that vibrational states should exhibit deviations from conventional spectroscopic models. According to the calculations, the effect of this interaction would critically depend on the type of the vibrational motion, being negligible for all vibrational states observed so far below 7920 cm^{-1} . Transitions measured in the present work reach a vibrational state near 7969 cm^{-1} which is sensitive to this predicted effect. Upper state assignments confirmed by the vibrational dependence of the rotational constants play a crucial role for the interpretation of related vibrational dynamics. A comparison of the obtained experimental data with *ab initio* calculations using single-well approximation and the three-wells approach is discussed in the conclusion, Sec. IV.

II. EXPERIMENT

Environmental applications and climate research impact have been an incentive for many laboratory studies of high-resolution spectra of ozone isotopic species (see [50–59] and references therein). The most relevant information concerning absorption spectra is included in the HITRAN [60] and GEISA [61] spectroscopic databases and collected in the web-accessible information system “Spectroscopy & Molecular Properties of Ozone” (SMPO) [53].

Most of spectra in the infrared ranging from fundamental to relatively strong overtone and combination bands with low and moderate vibration excitation are accessible by Fourier transform spectroscopy (FTS) [50–54]. In terms of normal-mode quantum numbers, ν_i , this was limited to $\sum_i \nu_i \leq 6$, i.e. to band centers below 5600 cm^{-1} ($\nu_{i=1-3}$ are the conventional vibrational normal-mode quantum numbers corresponding to the symmetric stretching, bending, and antisymmetric

stretching modes, respectively; the corresponding fundamental wave numbers are about 1103, 701, and 1042 cm^{-1} , respectively). Due to the rapid decrease of absorption intensities of the vibrational bands at increasing wave numbers (see Fig. 2 of Ref. [62]), the FTS technique does not provide the required sensitivity to access vibrational levels approaching the dissociation threshold. Highly sensitive laser techniques [63–74] are required to probe rovibrational states towards D_0 . In a series of previous works by cavity-ring-down spectroscopy (CRDS), we investigated systematically the 5850–7920- cm^{-1} spectral region [64–74]. More than 30 vibrational bands of $^{16}\text{O}_3$ were rovibrationally assigned and modelled using the effective Hamiltonian approach. The analyses of the corresponding bands provided a set of more than 5000 rovibrational levels. As mentioned above, their comparison with *ab initio* potential energy surface (PES) [15] gave experimental insight [62] into the long-standing “reef structure” issue [15,25–27,36,38,39] of the PES shape in the transition state.

Compared to our previous CRDS studies of ozone below 7920 cm^{-1} , the present use of an external cavity diode laser (ECDL) instead of a series of fibered distributed feedback (DFB) allows for a more efficient light injection into the CRDS cell and thus for an improved sensitivity. These improved performances are necessary to detect the extremely weak ozone bands located around 8000 cm^{-1} . The same setup was recently used to characterize the high-energy part of the O_2 band at 1.27 μm [75] and extremely weak transitions in the 1.18- μm window of CO_2 [76]. From recordings with noise equivalent absorption, α_{min} , on the order of a few 10^{-12} cm^{-1} , lines among the weakest ever reported (intensity as low as 5×10^{-31} $\text{cm}/\text{molecule}$) could be measured [75,76]. In the following, we recall the different parts of the setup and the procedure adopted for the recording of the ozone spectra.

A. The CRDS spectrometer

The heart of the spectrometer is a high-finesse optical resonator made of a stainless tube fitted with two highly reflective mirrors on its extremities, one of them being mounted on a piezoelectric element PEE_C , that allows the cavity length to be slightly length modulated. To limit the gas temperature gradients, this sample cell was covered with a tube of insulation foam and placed inside a Plexiglas enclosure. The stainless tube temperature was continuously monitored with an analog temperature sensor (TSic 501, IST-AG, ± 0.1 K accuracy). The sample pressure in the cell was continuously monitored with a 1000-Torr capacitance gauge (MKS Baratron, 0.15% accuracy of the reading). During the various days of the measurement campaign the temperature varied between 293.8 and 294.1 K.

The reader is referred to Konefal *et al.* (in particular its Fig. 2) [75] for a detailed description of the CRDS setup, except that, for the sake of a faster scan rate, we did not implement the optical frequency comb referencing or disciplining. Briefly, the ECDL light is first sent into a polarization maintained fiber coupler (PFC, 90/10), which directs about 10% of the emitted light to a Fizeau wave meter (High Finesse WS-U-30 IR, 5 MHz resolution, 20 MHz accuracy) and the remaining 90% into a fibered acousto-optic modula-

tor (AOM) inserted before the 1.4-m-long high-finesse cavity (HFC) ($F \approx 200\,000$). The AOM, used on its order +1, interrupts the excitation once resonance with one of its longitudinal modes is achieved, leading to a ring-down (RD) event. Each RD is detected with an InGaAs photodiode. The resonance is sought by adjusting the length of the cavity over $\lambda/2$ with PEE_C , hosting the output mirror.

The cavity losses at each laser wavelength were obtained by averaging the results of exponential fits to some tens of ring-down events, thus giving one data point in the spectrum. The absorption coefficient $\alpha(\text{cm}^{-1})$ was then directly calculated from the decrease of the cavity ring-down time τ (in s) induced by the molecular absorption:

$$\alpha(\nu) = \frac{1}{c} \left(\frac{1}{\tau} - \frac{1}{\tau_0} \right), \quad (1)$$

where c is the light velocity and τ_0 is the ring-down time of the empty cell depending of the mirror transitivity, diffraction losses, volume scattering, etc.

The frequency emission of the ECDL (DL pro 1200 from Toptica) was tuned by acting on its internal grating angular position and the laser chip current, in an electronically controlled laser-current-feedforward scheme. The grating angular position can be roughly set with an external step motor and finely adjusted with an internal PEE_L . The ECDL has a mode-hop-free tuning range limited to 0.8 cm^{-1} obtained with a linear scan of the PEE voltage over about 80% of its full range capability. Broadband spectra were therefore obtained by concatenation of series of slightly overlapping individual narrow spectra. During automatic broadband acquisition, the laser frequency was iteratively stepped by about 0.5 cm^{-1} , by acting on the grating with the step motor. A mode-hop-free scanning situation was then automatically sought by adjusting the PEE ramp offset over successive fast (1 s) test scans. The instantaneous laser frequency and the Fizeau wave meter raw signals were used as mode hop free and monomode emission criteria, respectively. Once the optimal PEE_L voltage offset was determined, a 10-min-long, ~ 60 -MHz step-by-step scan was started. After each frequency jump, 80 RDs were acquired before a new frequency step. In all the recordings, the sampling step was chosen to be about 2×10^{-3} cm^{-1} to be compared to a half width at half maximum (HWHM) Doppler linewidth of about 7×10^{-3} cm^{-1} (220 MHz) and an ECDL emission linewidth of 150 kHz at 1 ms integration. Typically, the recording of a 5- cm^{-1} -wide spectral interval required about 1 h. Overall, the presently analyzed spectrum covers the 7925–8070- cm^{-1} interval located just above the 5850–7920- cm^{-1} -wide range previously studied with DFB lasers [64–74]. The most excited band of $^{16}\text{O}_3$ previously analyzed is centered at 7860 cm^{-1} [73].

The absolute calibration of the frequency axis as provided by the wave meter was refined using accurate line centers of O_2 lines that we recently reported with an accuracy of better than 10^{-4} cm^{-1} [65].

B. Ozone preparation

The ozone sample was prepared using a silent electric discharge (12 kV, 400 Hz) at liquid-nitrogen temperature (LNT = 77 K). This system described in Ref. [77] allows obtaining a quasicomplete conversion of oxygen to ozone after

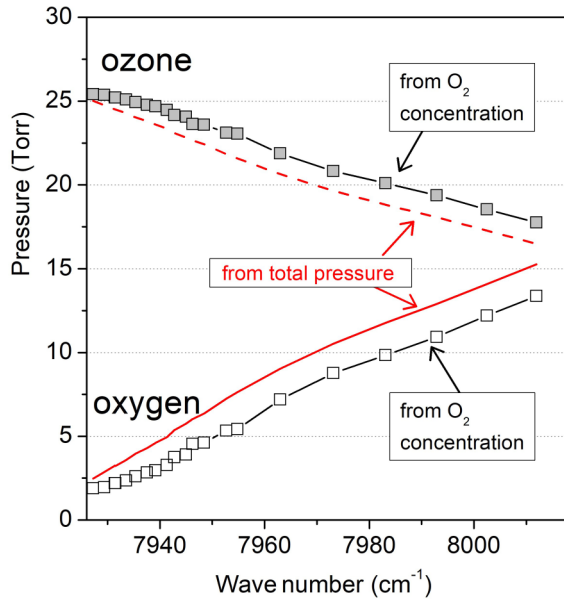


FIG. 1. Pressure variation due to the ozone decomposition in oxygen, during the CRDS recordings between 7920 and 8012 cm^{-1} . The ozone and oxygen partial pressures were determined in two independent ways: from the total pressure (dashed and solid red lines, respectively) and from the oxygen concentration derived from R -branch of the $a^1\Delta_g - X^3\Sigma_g^-(0-0)$ band of O_2 (grey and open squares, respectively).

a few minutes. First, the CRDS stainless-steel cell and the glass ozonizer connected with a glass tube were filled with oxygen (AlphaGaz2 from Air Liquide, purity $\geq 99.9995\%$) at a typical pressure of $P_0 = 40$ Torr at room temperature. Then the ozonizer was immersed into a Dewar filled with liquid nitrogen and the discharge was switched on for a few minutes. The total pressure was observed to decrease with time during a few minutes as a result of the $3\text{O}_2 \rightarrow 2\text{O}_3$ conversion of oxygen to ozone, the latter being trapped in the ozonizer. At a residual pressure of 0.05 Torr, the discharge was interrupted and the Dewar was removed. Ozone was then evaporated leading to an initial pressure very close to $(2/3)P_0 \approx 26.6$ Torr of pure ozone.

The long duration required for the spectra recordings made the slow decomposition of ozone in oxygen a major issue. In order to slow down the decomposition, EPDM O-rings were used instead of Viton and their number was minimized. Vacuum grease was also avoided. The quantitative estimation of the ozone decomposition is generally obtained from the increase of the total pressure. As a result of the $2\text{O}_3 \rightarrow 3\text{O}_2$ reaction, a 1 Torr increase of the total pressure is expected to correspond to a 2 Torr decrease of the ozone partial pressure and the ozone partial pressure can be deduced from the total pressure P measured at each spectral point: $P_{\text{O}_3} = 2(P_0 - P)$. The dependence of P_{O_3} versus the wave number, i.e. versus time (as the scanning speed of the laser frequency was constant), is presented in Fig. 1. During the 26-h duration of the recordings of the displayed 7920–8012- cm^{-1} region, the ozone partial pressure was observed to decrease mostly linearly with time from 26 to 17.6 Torr, with a decomposition rate of 0.2 Torr/h. This value which is about two orders of

magnitude larger than reported by Suzuki *et al.* [78] for a trace of ozone diluted in oxygen indicates that in our setup, some highly reactive elements [*e.g.* parts of the piezoelectric transducer (PZT)] remain and rule the ozone oxidation.

Figure 1 includes the oxygen partial pressure dependence obtained from $P_{\text{O}_2} = 3P - 2P_0$. Interestingly, the range of the present recordings makes possible an independent determination of the oxygen partial pressure and thus to check the above pressure values. Indeed, the studied spectral interval covers part of the R -branch of the $a^1\Delta_g - X^3\Sigma_g^-(0-0)$ band of O_2 centered at 1.27 μm . The corresponding oxygen lines can be used to determine the oxygen concentration. The resulting oxygen partial pressures deduced from the O_2 lines are plotted in Fig. 1 together with the corresponding ozone partial pressures obtained by difference from the measured total pressure. (Note that we derived the O_2 concentration using the line intensity values recently reported in Ref. [75] which correct HITRAN values by 2–4%.)

The two pressure determinations lead to similar wave number (*e.g.* time) dependencies and an overall satisfactory agreement except for a mostly constant difference of about 1.2 Torr on P_{O_3} . Although limited, the origin of this discrepancy is not fully understood. It could be due to chemical reactions of ozone with surface elements leading to different products than the O_3 to O_2 conversion, as illustrated by the observed impurity lines (see below).

For the ozone line intensity retrieval presented below, we adopted the same method as in our preceding works and used the ozone partial pressure value as calculated from the total pressure. The 1.2-Torr difference between the two P_{O_3} determinations represents a fraction of P_{O_3} increasing from 4.5% to 7% over the 7920–8012- cm^{-1} region. This uncertainty on P_{O_3} was taken into account in the overall error bar on the intensity values ($\sim 12\%$, see below).

In the following, for the convenience of the data treatment, the obtained absorption coefficients were normalized to an arbitrary constant ozone pressure (10.0 Torr).

C. Impurities and line parameters retrieval

An important difficulty of the spectrum treatment is related to the superposition of many impurity lines to the targeted ozone spectrum. In fact, as illustrated in Fig. 2, the spectrum is largely dominated by lines due to oxygen, water, CO_2 , and HF. During the recordings, the molar fraction of the impurities varies according to the ozone decomposition, desorption, or chemical reactions with the walls of the setup. The most probable sources are the following: water is desorbing from the gas cell, HF is probably coming from reaction with O-rings, and CO_2 might be due to a surface reaction with stainless steel.

The strongest ozone lines observed in the region have an intensity on the order of 2×10^{-28} cm/molecule, which is to be compared to maximum intensity values on the order 5×10^{-26} , 5×10^{-25} , 2×10^{-26} and 3×10^{-20} cm/molecule for oxygen, water, CO_2 , and HF, respectively. These values lead to molar fractions of water, CO_2 , and HF, on the order of 10^{-3} , 2×10^{-3} and 10^{-5} at most, respectively, and thus with negligible contribution to the total pressure. Due to the ozone decomposition, oxygen partial pressure can be on the same

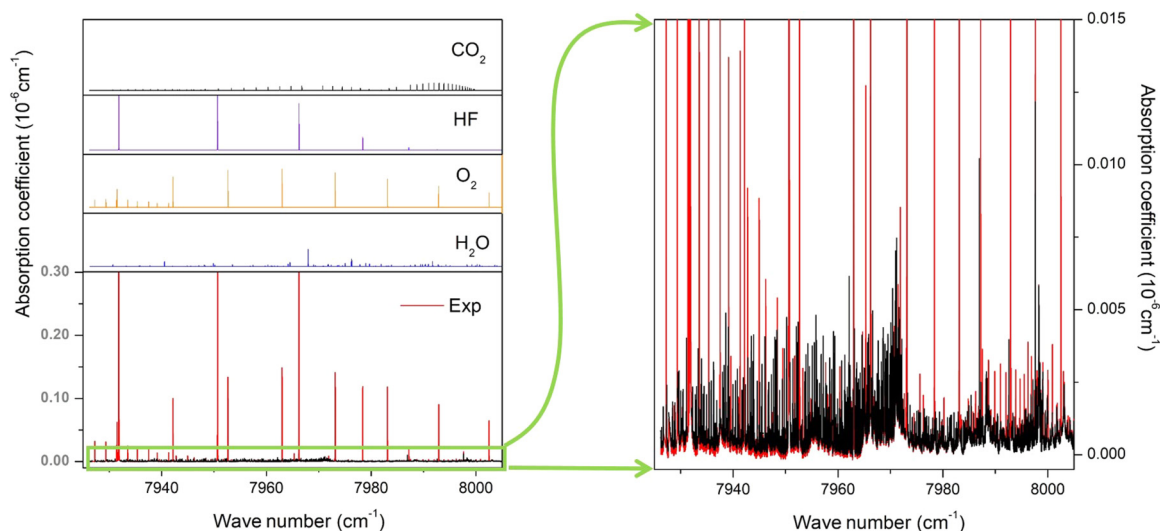


FIG. 2. Overview of the CRDS ozone recordings between 7925 and 8010 cm^{-1} . Left panels: Due to the weakness of the ozone spectrum, the recorded spectrum (lower panel) is dominated by impurity lines. The contributions of oxygen, water, CO_2 , and HF are simulated using the HITRAN database with rough estimated concentrations. CRDS spectrum of ozone was normalized at the ozone pressure of 10 Torr. Right panel: Enlargement of the ordinate scale by a factor of about 20 showing ozone bands (in black) superimposed with the simulated contributions of the impurity species (in red).

order as the ozone partial pressure at the end of the spectra recording (see Fig. 1).

Due to the extension and congestion of the spectrum, an accurate and systematic removal of the impurity lines from the spectrum after a careful line-by-line fit of all the absorption features was not systematically undertaken. This laborious work was limited to small spectral intervals around ozone lines which were rovibrationally assigned (see below). Nevertheless, an automatic program using as starting point a spectrum simulation using the HITRAN line lists [60] of the various impurity species with concentration dynamically adjusted according to the wave number was elaborated in order to highlight the ozone contribution to the recorded spectra. The results of the procedure are presented on the right panel of Fig. 2. After subtraction of the impurities contribution, two ozone A -type bands showing a bandhead near 7973 and 7998 cm^{-1} are clearly apparent. The corresponding rovibrational assignments will be described in the following sections. It is interesting to note that the strongest absorption feature observed on the “cleaned” spectrum at about 7997.6 cm^{-1} is an ozone line belonging to the ${}^3A_2(0, 0, 0) - X(0, 2, 0)$ hot band of the Wulf electronic system. This rovibronic band centered at about 8154 cm^{-1} is predissociated but shows a series of narrow absorption lines which extends down to 8000 cm^{-1} and will be the subject of a separate study (see Refs. [79,80] for an analysis of a similar hot band in ${}^{18}\text{O}_3$).

Line parameters were determined for most of the ozone lines which could be rovibrationally assigned. The line centers and line intensities were obtained by using a homemade interactive least-squares multilines fitting program written in LABVIEW. As the ECDL linewidth is much smaller than the Doppler broadening, the contribution of the apparatus function to the observed profiles was neglected. The fits were done over narrow spectral intervals including the assigned ozone lines and overlapping lines (unassigned ozone lines or impurities) which could be fitted independently. For each spectral

interval, the line center, integrated absorption coefficient, and Lorentzian width of each line as well as the baseline (assumed to be a linear function of the wave number) were provided by the fitting procedure. The Doppler broadening was fixed according to the mass of the species and the temperature of the gas. The Lorentzian width was fitted when possible or fixed to a value calculated from the default value of 0.09 $\text{cm}^{-1}/\text{atm}$ provided by the HITRAN database for self-broadening coefficient of ozone. Note that in our pressure conditions (about 25 Torr), the Lorentzian width ($\sim 3 \times 10^{-3} \text{cm}^{-1}$ HWHM) is about half the Doppler line width ($7 \times 10^{-3} \text{cm}^{-1}$).

The difficulty of the line parameter derivation due to the considerable spectral congestion is illustrated in Fig. 3 in a spectral interval near 7948 cm^{-1} . The simulation based on the retrieved line parameters (middle panel) is compared to the experimental spectrum. The contribution of impurity lines (water and CO_2) is accounted for, and the (expt.-sim.) residuals (lower panel) correspond to a root-mean-square deviation of about 10^{-11}cm^{-1} . The rovibrational lines of ozone which could be assigned in the displayed region are indicated.

The line intensity, S_{ν_0} , of a rovibrational transition centered at ν_0 was obtained from the integrated absorption coefficient A_{ν_0} ($\text{cm}^{-2}/\text{molecule}$):

$$A_{\nu_0} = \int_{\text{line}} \alpha_{\nu} d\nu = S_{\nu_0}(T)N, \quad (2)$$

where ν is the wave number in cm^{-1} , α_{ν} is the absorption coefficient in cm^{-1} obtained from the cavity ring-down time [Eq. (1)], and N is the volume number density in $\text{molecule}/\text{cm}^3$ obtained from the pressure and temperature values. In the favorable cases of well isolated and relatively strong lines (we are speaking about line intensities on the order of only a few $10^{-28} \text{cm}^2/\text{molecule}$!), the accuracy of the line positions is estimated to be about 10^{-3}cm^{-1} . Because of the moderate signal-to-noise-ratio, the statistical error of the fit leads to error bars on the integrated absorption coefficient

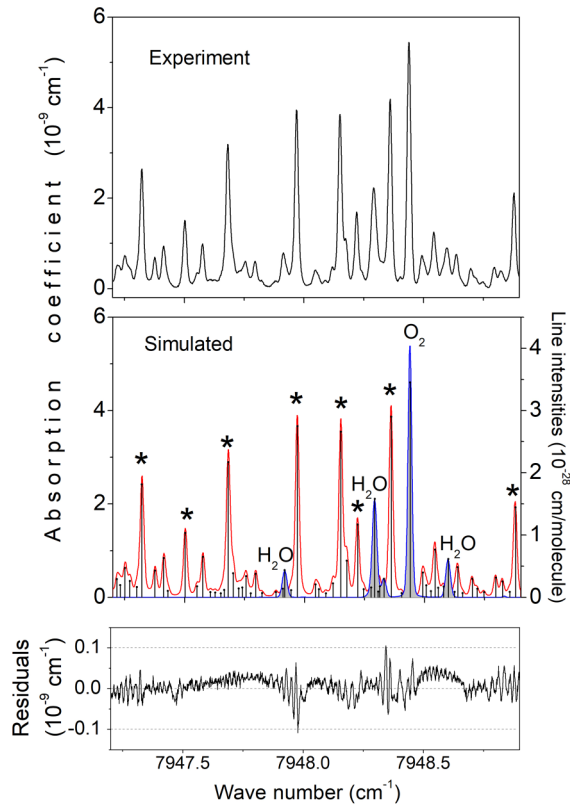


FIG. 3. Example of line parameters retrieval near 7948 cm^{-1} . Upper panel: CRDS spectrum normalized at an ozone pressure of 10 Torr. Middle panel: Absorption simulation based on the retrieved line parameters and corresponding stick spectrum. The impurity lines (water and O_2) are indicated. The rovibrational lines of $^{16}\text{O}_3$ assigned in this work are marked by asterisks. Lower panel: (expt.-sim.) residuals. The corresponding *rms* deviation is about 10^{-11} cm^{-1} .

of about 3–5%. Nevertheless, taking into account frequent line overlapping and the above discussed uncertainty of the ozone partial pressure, we estimate to 10–15% the average value of the reported obtained intensity values. This is comparable or even a better precision with respect to what was previously achieved in some lower wave number ranges.

III. ANALYSES AND RESULTS

In lower energy ranges, two types of ozone vibration-rotation bands have been observed, as reviewed in [50–53]. The strongest ones are activated due to the component of the dipole moment which is parallel to the a axis of the principal inertia moment. Such bands, usually called “parallel” bands or A -type band, follow the selection rules $\Delta v_3 = \text{odd}$ and $\Delta K_a = \text{even}$. The second type of bands are the “perpendicular” bands or B -type bands which follow the selection rules $\Delta v_3 = \text{even}$ and $\Delta K_a = \text{odd}$. Within the same frequency interval, these latter bands are usually weaker and have quite irregular line intensity patterns making more difficult their rovibrational assignment. Due to their weakness and irregular structure, dipole absorption perpendicular bands have not been assigned in wave number ranges above 6770 cm^{-1} [52,73]. However, the corresponding upper states play the

role of “dark” states which may perturb the observed “bright” states *via* accidental resonance interactions [52].

Many previous studies have made it clear that vibrational extrapolation using standard Dunham-type expansion [81] in terms of quantum numbers v_1, v_2, v_3 does not give reliable results for the ozone band centers near the dissociation threshold. In this work, the identification of new bands in the recorded CRDS spectrum relied on the variational predictions from the *ab initio* PES reported in Ref. [15] where the “global” vibrational assignment (Γ, N) was given by the irreducible representation Γ of C_{2v} point group and the ranking number N , increasing with energy.

In the $7920\text{--}8000\text{ cm}^{-1}$ range of the present recordings, eight vibrational levels of A_1 and B_1 types in the C_{2v} point group are predicted [15]. Four of them - $N = 87\text{--}90$ at $7928.76, 7944.73, 7971.69,$ and 7991.66 cm^{-1} , respectively - belong to the B_1 irreducible representation (antisymmetric with respect to the C_2 axis). Note that for B_1 vibrational levels, $J = 0$ states are not spin-allowed [51,52] because all ^{16}O nuclei of the main ozone isotopologue, $^{16}\text{O}_3$, are bosons. However, the calculation of such states, *via* the diagonalization of *ab initio* based vibrational Hamiltonian, is meaningful because they correspond to observable band centers obtained as the $J \rightarrow 0$ limit of experimental rotational line series. The $J > 0$ rovibrational states of B_1 vibrational levels do exist and the transitions to these states correspond to parallel ($A_1^{\text{vib}} \rightarrow B_1^{\text{vib}}$) bands, which are determined experimentally. Another four vibration levels belonging to totally symmetric A_1 irreducible representation are predicted [15]: $N = 117\text{--}120$ at $7943.73, 7949.28, 7957.30,$ and 7971.01 cm^{-1} , respectively. They could give rise to very weak perpendicular ($A_1^{\text{vib}} \rightarrow A_1^{\text{vib}}$) bands with hardly assignable tiny and irregular patterns, which do not exhibit characteristic bandheads [52].

As in previous studies [62,82], to help the assignment, the rovibrational $J = 1$ and $J = 2$ levels were computed from the *ab initio* PES [15] and used to determine theoretical values of $A_V, B_V,$ and C_V rotational constants of the different predicted vibrational states. Their comparison with observations will be discussed in Sec. IV.

A. Spectra assignment

The effective Hamiltonian (EH) and effective dipole moment (EDM) models were used for the assignments. The basic definitions and technical details can be found in Refs. [50–53]. The iterative fits of measured line positions and line intensities and the elaboration of the calculated line lists used the GIP program [83]. At the initial iteration, *ab initio* values [15] were adopted for the band centers and for rotational constants involved in the EH model as adjustable parameters. This allows us to follow series of lines with increasing total rotational quantum number J for various values of K_a . In general, the $(v_{\text{obs}} - v_{\text{calc}})$ position difference *versus* rotational quantum numbers showed a smooth dependence until a resonance perturbation appears. A comparison of the corresponding deviation curves as a function of K_a permits assigning a few lines with J values corresponding to relatively large intensities ($J \sim 6\text{--}15$). A second way, particularly relevant for A -type bands in the CRDS spectral range, was to look at the sharp

observed bandhead in the R branch, trying various assignments and seeking the same ($\nu_{\text{obs}} - \nu_{\text{calc}}$) residuals in the P branch. Successive fits of EH parameters allowed us to assign more and more lines by iterations.

One well-known difficulty was the modeling of irregular deviations from a single-vibration-state model, which appears to be due to perturbations caused by resonance interactions with dark states. This problem becomes increasingly complicated to solve at high-energy where the density of rovibrational states drastically increases towards the dissociation threshold.

Another issue was that rotational series of lines behaved in a different way depending on the parity of J and on values of $K_a = 1, 2$, and 3 , etc. To extend the assignments at the initial step of the analyses, effective parameters specific for these different J, K_a series were determined. This can be seen as an experimental confirmation of the effect of the interaction between three potential wells on rovibrational band patterns. Indeed, the recent study by Kokouline *et al.* [18] predicted from symmetry considerations using global *ab initio* PES that rovibrational bands of ozone should split into subbands depending on J, K_a, K_c at high energies. This is because the vibrational wave functions, which are localized in the three wells at low energies, can be mixed by tunneling effects [18] near D_0 , though a direct measurement of the splitting values is not allowed by the spin statistics.

This observation represents a challenge for further developments of theoretical EH models in the case of coupled potential wells, as the available spectroscopic models for experimental data reduction [50–52], which have been worked out in a frame of the one-well approximation, did not account for this effect. Consequently, the *rms* fit deviation using available EH models increases, whereas rotational constants take average values among J, K_a series and have to be interpreted as expectation values of the inverse inertia moments in the corresponding vibrational wave functions [17,18]. Interestingly, such irregular J, K_a behavior is much more pronounced for the $\nu_1 + 6\nu_2 + 3\nu_3$ band (Sec. III B) than for the $6\nu_1 + \nu_2 + \nu_3$ band (Sec. III C): the *rms* fit deviation for the first band is about five times larger than for the second one. A plausible explanation of this observation from the point of view of vibrational dynamics is discussed in the conclusion, Sec. IV.

As far as possible, ground-state combination differences (GSCDs) relations from transitions belonging to P, R , or Q branches were checked to ensure the assignments providing thus reliable information independently of a shortcoming of EH models. In addition, we also verified that relative intensities calculated with an approximate value of the fitted effective dipole moment were qualitatively consistent with the observations, thanks to synthetic spectra computed by the MULTIFIT program [84].

B. The $\nu_1 + 6\nu_2 + 3\nu_3$ band in the 7930–7973 cm^{-1} range

The position of the bandhead observed at 7973 cm^{-1} (see Fig. 2) points the $(B_1, N = 89)$ upper state at 7971.69 cm^{-1} as the most probable candidate for the upper state of the corresponding parallel band. This is consistent with simulations using *ab initio* values of the corresponding rotational constants which indicate that the center of the observed band

should lie about 2–3 cm^{-1} below the sharp absorption feature of the bandhead. The $(B_1, 89)$ upper vibration level is assigned as $(\nu_1, \nu_2, \nu_3) = (1, 6, 3)$. This vibrational assignment relies on the decomposition of the corresponding *ab initio* wave function in the normal-mode basis set using the contact transformation (CT) method. To this end, we used the MOL_CT program suite [85,86]; the technical aspects of calculations were described in [82,85,86].

1. Line positions and energy levels

The first series of assignments concerning the $K_a = 4$ upper state levels was validated by GSCD relations involving the P, Q , and R branches. Then, a similar procedure was applied to other K_a values leading to the assignment of 243 transitions of the $\nu_1 + 6\nu_2 + 3\nu_3$ band reaching a total of 130 upper state energy levels. The experimentally determined energy levels are listed in Table I with their corresponding statistical error bars when they could be derived from different transitions.

A fit of the experimental line positions using an isolated state EH model leads to an *rms* deviation of 0.148 cm^{-1} , largely above the experimental uncertainty. Deviations between measured and calculated position values were found to be either positive or negative, depending on the parity of J , without smooth dependence on rotational quantum numbers. Particular large perturbations were detected for $K_a = 1$ and 2 series. The introduction of a Coriolis interaction with the $(A_1, 118)$ dark state predicted at 7949.28 cm^{-1} [15] allowed for a reduction of the *rms* deviation by a factor of 2 (0.078 cm^{-1}). The set of derived parameters is given in Table II. Note that the mixing coefficient between $J, K_a, K_c = 14, 2, 13$ of the $(B_1, 89)$ state and $J, K_a, K_c = 14, 3, 11$ of the $(A_1, 118)$ state is about 50–50 % making the labelling of this particular rovibrational level ambiguous. This type of strong mixing has already been observed at lower energy (see for instance Ref. [87]).

2. Line intensities and effective dipole transition moment

The empirical determination of weak band transition moments from crowded spectra is quite sensitive to uncertainties of experimental intensities and to the completeness of underlying theoretical model. Among the assigned transitions of the $\nu_1 + 6\nu_2 + 3\nu_3$ band, a subset of 182 relatively isolated lines sampling the P, Q , and R branches was selected. Depending on the proximity with other lines, realistic error bars were evaluated and associated to the corresponding line intensities. The intensity values were used as input data of a weighted fit of the EDM parameters. The standard EDM model for A -type bands of C_{2v} molecules was adopted [90,91]:

$$\begin{aligned} \langle V''(V') | \tilde{\mu}_Z^{(A)} | V''(V') \rangle = & d_1^A \varphi_z + d_2^A \{\varphi_z, \mathbf{J}^2\} + d_3^A \{\varphi_z, J_z^2\} \\ & + d_4^A \frac{1}{2} [\{\varphi_x, iJ_y\} - \{i\varphi_y, J_x\}] \\ & + d_5^A \frac{1}{2} [\{\varphi_x, J_x J_z + J_z J_x\} - \{i\varphi_y, i(J_y J_z + J_z J_y)\}] \\ & + d_6^A \frac{1}{2} [\{\varphi_x, iJ_y\} + \{i\varphi_y, J_x\}] + \dots, \quad (3) \end{aligned}$$

where the notation $\{X, Y\} = XY + YX$ stands for an anticommutator, φ_α are direction cosines for the Eckart molecular fixed frame, J_α is the molecular fixed component of the total

TABLE I. Rovibrational energy levels derived from observed transitions for the (1,6,3) and (6,1,1) vibration states of $^{16}\text{O}_3$.

J	K_a	K_c	(1,6,3)			(6,1,1)			J	K_a	K_c	(1,6,3)			(6,1,1)		
			E (cm $^{-1}$)	Nb	ΔE	E (cm $^{-1}$)	Nb	ΔE				E (cm $^{-1}$)	Nb	ΔE	E (cm $^{-1}$)	Nb	ΔE
1	0	1	7969.5294	1		7993.6164	1		13	2	11	8049.7297	2	0.1	8077.0688	1	
1	1	0				7996.6583	2	0.0	13	3	10	8064.2333	2	0.2	8091.8783	2	0.8
2	1	2	7974.0368	1		7998.1394	2	1.2	13	4	9	8085.6814	3	0.3	8112.4860	1	
2	2	1	7983.3140	1		8007.2677	1		13	5	8	8113.2495	3	0.2	8139.6000	2	0.9
3	0	3	7973.2411	1		7997.5429	2	0.7	13	6	7	8146.9147	2	0.7	8172.5748	2	0.5
3	1	2				8000.7153	1		13	7	6	8186.7142	2	0.1			
3	2	1	7985.5595	2	0.3	8009.6269	2	0.1	14	1	14	8046.6396	2	0.2	8075.5942	1	
3	3	0	8000.9057	1		8024.7016	2	0.2	14	2	13				8087.2677	2	0.2
4	1	4	7979.1191	2	0.1	8003.4646	1		14	3	12	8074.6230	1		8102.8590	1	
4	2	3	7988.5467	1		8012.7694	3	0.3	14	4	11	8096.1139	2	0.2	8123.4674	2	0.6
4	3	2	8003.8791	3	0.3	8027.7930	1		14	5	10	8123.6803	3	0.7	8150.5991	2	0.1
4	4	1	8025.3594	1		8048.9209	1		14	6	9	8157.3485	2	0.5	8183.5544	2	0.5
5	0	5	7979.9085	2	0.0	8004.6010	2	0.6	14	7	8	8197.1597	2	0.1			
5	1	4	7983.4015	2	0.1	8008.0042	1		15	0	15	8056.4647	2	0.0	8085.8301	2	0.2
5	2	3	7992.3147	2	0.3	8016.7197	3	0.5	15	1	14	8063.7405	2	0.0	8092.6683	2	0.4
5	3	2	8007.5955	1		8031.6599	2	0.1	15	2	13	8071.8674	2	0.1	8100.2682	1	
5	4	1	8029.0788	1		8052.8445	2	0.2	15	3	12	8085.9023	2	0.1	8114.7291	1	
5	5	0	8056.6525	2	0.4	8079.8977	1		15	4	11	8107.3017	3	1.0	8135.2315	1	
6	1	6	7987.1440	2	0.6	8011.8310	2	0.5	15	5	10	8134.8562	3	1.5	8162.3864	2	0.8
6	2	5	7996.7518	3	0.1	8021.4119	2	1.0	15	6	9	8168.5267	2	0.7	8195.2969	3	0.9
6	3	4	8012.0628	1		8036.2627	1		15	7	8	8208.3566	2	0.6			
6	4	3	8033.5441	3	0.7	8057.5532	2	0.5	16	1	16	8069.2015	2	0.2	8099.0372	1	
6	5	2	8061.1204	2	0.2	8084.6104	1		16	2	15				8111.5025	2	0.6
6	6	1	8094.7657	1		8117.5858	1		16	3	14	8097.7524	2	0.6	8127.2479	2	0.0
7	0	7	7989.5056	1		8014.7591	1		16	4	13	8119.2302	2	0.0			
7	1	6	7993.3939	2	0.2	8018.5229	2	0.1	16	5	12	8146.7797	3	0.8	8174.9631	2	0.1
7	2	5	8002.0477	2	0.6	8026.9860	2	0.5	16	6	11	8180.4505	2	0.9			
7	3	4	8017.2666	2	0.4				16	7	10	8220.3162	2	1.6			
7	4	3	8038.7549	2	0.0	8063.0481	2	0.1	17	0	17	8080.2014	2	0.0	8111.0405	1	
7	5	2	8066.3336	1		8090.1066	3	0.2	17	1	16	8088.8058	2	0.2	8119.1313	1	
7	6	1	8099.9823	2	0.3	8123.0871	1		17	2	15	8097.1639	2	0.5	8126.7428	1	
7	7	0	8139.7261	1					17	3	14	8110.6071	2	0.3	8140.7770	2	0.3
8	1	8	7997.8048	1		8023.2820	2	0.0	17	4	3	8131.9187	1				
8	2	7	8007.9584	1		8033.1941	2	0.4	17	5	12	8159.4508	2	0.2	8188.3177	1	
8	3	6	8023.1759	2	0.1	8048.6488	1		17	6	1	8193.1237	2	0.4			
8	4	5	8044.7091	1		8069.3261	3	0.3	17	7	0	8232.9711	1				
8	5	4	8072.2890	2	0.3	8096.3904	2	0.3	18	1	18	8093.4451	1		8125.4869	1	
8	6	3	8105.9426	2	0.2	8129.3746	2	0.8	18	2	17				8138.8183	1	
8	7	2	8145.6921	3	0.7				18	3	16	8123.8834	2	0.4	8154.7910	1	
9	0	9	8001.9979	1		8027.9996	2	0.3	18	4	15	8145.3442	2	0.6			
9	1	8	8006.4413	2	0.3	8032.2651	2	0.4	18	5	14	8172.8712	1		8202.4610	2	0.5
9	2	7	8014.8527	2	0.4	8040.4497	1		18	6	13	8206.5448	2	0.4			
9	3	6	8029.9235	2	0.4	8055.7098	3	0.6	18	7	12	8246.4216	1				
9	4	5	8051.4112	2	0.4	8076.3875	2	0.0	19	0	19	8106.7415	2	0.5	8139.1848	1	
9	5	4	8078.9957	1		8103.4616	3	0.4	19	1	18	8116.7904	1				
9	6	3	8112.6463	2	0.5	8136.4454	3	0.5	19	2	17	8125.6173	2	0.0	8156.4829	1	
9	7	2	8152.4021	3	0.4				19	3	16	8138.3634	2	0.1	8170.0370	1	
10	1	10	8010.7210	1		8037.6875	2	0.7	19	4	15	8159.5516	1				
10	2	9	8022.1628	2	0.0	8048.1028	2	0.7	19	5	14	8187.0380	2	0.4	8217.3867	1	
10	3	8	8037.3507	2	0.1	8063.5567	2	0.5	19	6	13	8220.7143	2	0.1			
10	4	7	8058.8605	1		8084.2362	2	0.3	20	1	20	8121.3250	1				
10	5	6	8086.4358	3	0.1	8111.3170	3	0.2	20	2	19				8169.1989	2	0.5
10	6	5	8120.0957	2	0.7	8144.3052	1		20	3	18	8153.0237	2	0.1	8185.4851	1	
10	7	4	8159.8598	2	0.0				20	4	17	8174.4616	2	0.0			
11	0	11	8017.3447	2	0.2	8044.2821	2	0.4	20	5	16	8201.9579	2	0.5	8233.0670	1	
11	1	10	8022.5294	2	0.2	8049.2157	2	0.3	20	6	15	8235.6359	2	0.1			

TABLE I. (Continued.)

J	K_a	K_c	(1,6,3)			(6,1,1)			J	K_a	K_c	(1,6,3)			(6,1,1)		
			E (cm ⁻¹)	Nb	ΔE	E (cm ⁻¹)	Nb	ΔE				E (cm ⁻¹)	Nb	ΔE	E (cm ⁻¹)	Nb	ΔE
11	2	9	8030.7350	2	0.4	8057.1341	2	1.1	20	7	14	8275.5665	2	0.5			
11	3	8	8045.5758	2	0.2	8072.2030	1		21	0	21	8136.3201	2	0.3	8170.2547	2	0.2
11	4	7	8067.0537	2	0.5	8092.8695	3	0.7	21	1	20	8147.6594	2	0.3			
11	5	6	8094.6283	3	0.3	8119.9577	3	0.3	21	2	19	8157.2112	2	0.0			
11	6	5	8128.2870	1		8152.9438	2	0.0	21	3	18	8169.1961	2	0.4	8202.5291	1	
11	7	4	8168.0643	1					21	5	16	8217.6239	3	1.2			
12	1	12	8027.2777	2	0.0	8055.1341	1		21	6	15	8251.3031	1				
12	2	11	8039.4034	2	0.0	8066.1303	2	0.2	22	2	21				8202.6317	2	1.3
12	3	10	8054.4907	2	0.4	8081.6279	2	0.0	22	3	20	8185.1884	2	0.2	8219.3199	2	0.2
12	4	9	8075.9933	3	0.2	8102.2870	2	0.7	22	5	18	8233.9755	1				
12	5	8	8103.5671	3	0.9	8129.3868	3	0.2	23	0	23				8204.2476	2	0.5
12	6	7	8137.2301	3	0.6	8162.3699	1		23	3	20				8238.2803	1	
12	7	6	8177.0147	2	0.9				24	3	22				8256.2835	1	
13	0	13	8035.5106	2	0.3	8063.5688	2	0.3	25	3	22				8277.2962	2	0.7
13	1	12	8041.6376	2	0.0	8069.3585	2	0.4									

Notes: Nb is the number of observed transitions used to determine the upper energy level E (cm⁻¹). ΔE is the *rms* error of the experimental energy determination (in 10⁻³ cm⁻¹ unit).

angular momentum, and $d_i^{(A)}$ are band-specific transition moment parameters empirically retrieved from the line intensities of the observed band. Five parameters of the effective dipole transition moment could be well determined with a weighted standard deviation of 1.061 and an *rms* deviation of 12%.

The results of the fit are provided as Supplemental Material [92] together with the diagrams of comparison between the measured and calculated intensities, while the derived EDM parameters are included in Table II together with corresponding fit statistics.

3. Comparison of simulated spectra with observations

A set of 366 calculated transitions of the $\nu_1 + 6\nu_2 + 3\nu_3$ band following the $\Delta K_a = 0$ selection rule was generated using the EH and EDM parameters of Table II. The calculated set was limited to transitions reaching experimentally determined upper state levels and line positions were empirically corrected according to the experimental value of the upper energy levels listed in Table I. Line intensities were computed using the fitted EDM parameters and wave functions corresponding to the EH of Table I. Note that the resulting list

TABLE II. Spectroscopic parameters and fit statistics for the $\nu_1 + 6\nu_2 + 3\nu_3$ band of ¹⁶O₃ band centered at 7968.8 cm⁻¹.

(i) Spectroscopic parameters (cm ⁻¹)				(iii) Statistics for line positions	
	(1, 6, 3) \equiv (B_1 , 89)	(A_1 , 118)			
E^{VV}	7968.782 ₆ (18)	7949.76 ₁ (34)	J_{\max}		22
$A_V - (B_V + C_V)/2$	3.0769 ₈ (15)	3.164 ₆ (33)	$K_{a \max}$		7
$(B_V + C_V)/2$	0.37138 ₇ (18)	0.38564 ₄ (95)	Number of transitions		243
$(B_V - C_V)/2$	0.03044 ₄ (45)	0.0255 [f]	Number of levels		130
$\Delta_K \times 10^3$	0.300 ₉ (30)		<i>rms</i> (cm ⁻¹) ^a		0.078
$\Delta_{JK} \times 10^4$	-0.229 ₆ (39)		(iv) Statistics for line intensities		
$\Delta_J \times 10^5$	-0.152 ₃ (71)		J_{\max}		22
$\delta_J \times 10^5$	0.603 ₆ (52)		$K_a \max$		7
$\delta_K \times 10^3$	-0.203 ₃ (91)		Number of transitions		182
			<i>rms</i> (%) ^a		12.0
			$S_v = 4.18 \times 10^{-26}$ cm/molecule		
			at 296 K ^b		
Coriolis coupling between (A_1 , 118) and (1,6,3) states					
C_{011}	0.0172 ₅ (16)				
(ii) Dipole transition moment parameters (Debye)					
$d_1^{(A)} \times 10^5$	0.6028 ₄ (62)	$d_4^{(A)} \times 10^7$		-0.118 ₉ (16)	
$d_2^{(A)} \times 10^8$	-0.1568 ₄ (81)	$d_6^{(A)} \times 10^7$		0.390 ₃ (50)	
$d_3^{(A)} \times 10^8$	-0.397 ₄ (83)				

^a Two transitions to the upper state level $J, K_a, K_c = 21, 2, 19$ were excluded from the fit.

^b Sum of intensities in the combined line list (366 lines).

[f]: fixed to the values predicted from the PES of Ref. [15]. All higher-order centrifugal distortion parameters [88] quoted in [89] were held fixed to their ground-state values. Grey background corresponds to the ($\Gamma = A_1, N = 118$) dark state.

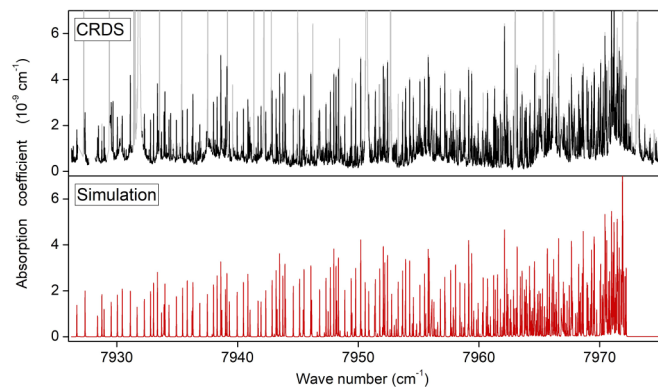


FIG. 4. Overview of the $\nu_1 + 6\nu_2 + 3\nu_3$ absorption band of $^{16}\text{O}_3$. Upper panel: CRDS spectrum with impurity lines (partly) removed at a pressure normalized to 10 Torr (the grey trace corresponds to the original CRDS spectrum with impurity lines whereas the ozone lines are shown in black). Lower panel: Simulation limited to transitions reaching experimentally determined upper levels with intensities computed from EH and EDM parameters (Table II) and line positions empirically corrected.

includes a number of lines unobserved in the spectrum (e.g., hidden by impurity lines) which have experimental accuracy on their line centers because they reach an upper level empirically determined from different transitions. The obtained line list provided as Supplemental Material [92] leads to the overview comparison presented in Fig. 4.

More detailed blown-up comparisons in the *P* and *R* branches are shown in Figs. 5 and 6. These figures provide extended qualitative validation of the assignments and of intensities computed from the fitted effective dipole transition moment parameters of Table II. They contain supplemental information concerning absorption features composed of doublet, triplet, and other overlapping lines, which were not possible to include in the dipole moment fit. The account for new computed transitions (beyond 182 intensities included in the fit) are particularly important for the *R* branch (Fig. 6) because they contribute to overlapping lines near the compressed bandhead, which corresponds to the strongest absorption features of the band.

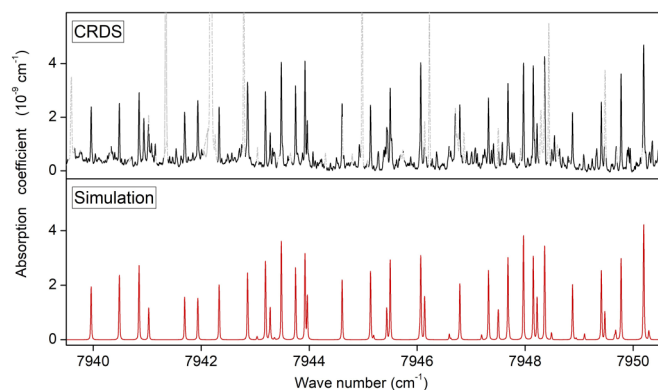


FIG. 5. Example of comparison of CRDS and simulated spectra in the *P*-branch region in the $\nu_1 + 6\nu_2 + 3\nu_3$ band. (see Fig. 4 for the panel descriptions).

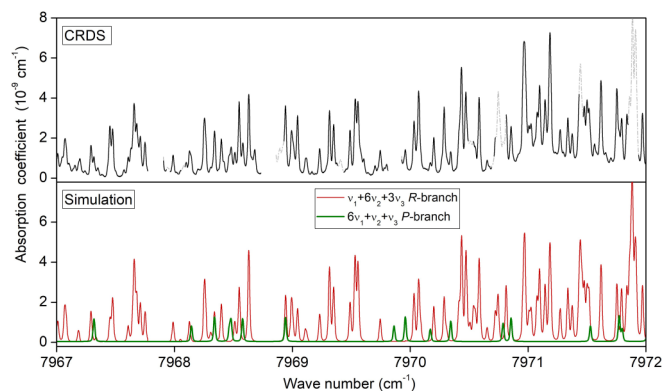


FIG. 6. Same as Figs. 4-5 in the *R*-branch region of the $\nu_1 + 6\nu_2 + 3\nu_3$ band. A few lines (green) correspond to a simulation of the *P* branch of the $6\nu_1 + \nu_2 + \nu_3$ band (see Sec. III C).

C. The $6\nu_1 + \nu_2 + \nu_3$ band in the range 7951–8000 cm^{-1}

A head of a weak vibration-rotation band is observed near 7998 cm^{-1} (Fig. 2). It is superimposed with H_2O impurity lines, and other ozone lines, in particular, with some strong absorption features due to vibronic transitions of the $^3A_2(0, 0, 0) - X(0, 2, 0)$ hot band of the Wulf electronic system, making the assignment more challenging. According to the *ab initio* predictions, the $(B_1, 90)$ vibrational level predicted at 7991.66 cm^{-1} [15] is the most plausible candidate for the upper state of this *A*-type band. This is confirmed by calculations using the theoretical values of rotational constants which predict a bandhead agreeing with the observations within about 1 cm^{-1} . The decomposition of the $(B_1, 90)$ *ab initio* wave function in the normal mode basis gives a major contribution to the $(\nu_1, \nu_2, \nu_3) = (6, 1, 1)$ normal-mode vibration. Consequently, the corresponding parallel absorption band was assigned as $6\nu_1 + \nu_2 + \nu_3$. Note that the low-energy neighbor of the $(B_1, 90)$ level - $(B_1, 89)$ - is the upper level of the $\nu_1 + 6\nu_2 + 3\nu_3$ parallel band assigned above, whereas the next parallel band, reaching the $(B_1, 91)$ level, is predicted 52 cm^{-1} [15] above the observed bandhead.

1. Line positions and energy levels

Following the above described procedures, 189 transitions of the $6\nu_1 + \nu_2 + \nu_3$ band corresponding to 110 upper state energy levels could be assigned. It appeared that the $K_a = 3$ series was strongly perturbed. Thanks to *ab initio* predictions [15], this perturbation was identified as a strong Coriolis resonance with the $K_a = 4$ levels of the $(A_1, 119)$ vibrational state predicted at 7957.30 cm^{-1} and confirmed by next assignments. The introduction of this dark state in the EH model permitted reducing the final *rms* deviation in line positions from 0.12 to 0.016 cm^{-1} . The fitted values of the spectroscopic parameters are given in Table III. The experimentally determined values of the $(6, 1, 1)$ rovibrational levels are included in Table I.

2. Line intensities and effective dipole transition moment

As for the previous band, a restricted set of relatively isolated lines were used for the determination of the EDM

TABLE III. Spectroscopic parameters and fit statistics for the $6\nu_1 + \nu_2 + \nu_3$ band of $^{16}\text{O}_3$ centered at 7992.6 cm^{-1} .

(i) Spectroscopic parameters (cm^{-1})			(iii) Statistics for line positions	
	(A1,119)	(6, 1, 1) \equiv (B_1 , 90)	J_{max}	25
E^{VV}	7962.623 ₅ (56)	7992.8307 ₅ (35)	$K_{a\text{max}}$	6
$A_V - (B_V + C_V)/2$	3.6674 [f]	3.02065 ₄ (42)	Number of transitions	189
$(B_V + C_V)/2$	0.37059 ₉ (77)	0.392989 ₅ (31)	Number of levels	110
$(B_V - C_V)/2$	0.0263 [f]	0.024256 ₉ (24)	rms (cm^{-1})	0.016
$\Delta_K \times 10^3$		0.400 ₃ (12)	(iv) Statistics for line intensities	
$\Delta_{JK} \times 10^5$		-0.32 ₇ (15)	J_{max}	18
$\Delta_J \times 10^6$		0.827 ₇ (50)	$K_a\text{max}$	6
Coriolis coupling term between (6,1,1) and (A1,119) (cm^{-1})			Number of transitions	67
C_{011}	-0.01954 ₅ (24)		rms (%)	15.5
			$S_V = 1.36 \times 10^{-26}$ cm/molecule	
			at 296 K ^a	
(ii) Dipole transition moment (Debye)				
$d_1^{(A)} \times 10^5$	0.3187 ₀ (26)			

^aSum of intensities in the combined list (306 lines).

[f]: fixed to the values predicted from the PES of Ref. [15]. All higher-order centrifugal distortion parameters [88] quoted in [89] were held fixed to their ground-state values. Grey background corresponds to the ($\Gamma = A_1$, $N = 119$) dark state.

parameters. Note that the weakness of the band (line intensities between 10^{-29} and 10^{-28} cm/molecule) results in larger uncertainties on the intensity values. Only the principal transition moment parameter could be determined from the weighted fit of 67 line intensities belonging to P , Q , and R branches (weighted standard deviation of 1.009 and rms deviation of 15.5% - see Table III and Supplemental Material [92]).

3. Comparison of simulated spectra with observations

In the same way as for the $\nu_1 + 6\nu_2 + 3\nu_3$ band, a set of calculated transitions reaching the experimentally determined energy level of the (6,1,1) state was generated. Line positions were adjusted according to the experimental energy values (Table I) while line intensities were computed using the EDM parameters and EH eigenfunctions (Table III). The list provided as Supplemental Material [92], includes 306 transitions up to $J_{\text{max}} = 25$, $K_{a\text{max}} = 6$. The sum of their calculated intensities is $S_V = 1.3 \times 10^{-26}$ cm/molecule, a factor of 3 smaller than for the $\nu_1 + 6\nu_2 + 3\nu_3$ band.

Figures 7 and 8 show an overview comparison of the simulated absorption coefficient using this combined line list of the $6\nu_1 + \nu_2 + \nu_3$ band (lower panel) to the CRDS spectrum (upper panel) in the P and R branch region, respectively. Let us note that the CRDS spectrum is formed by narrow rovibrational lines superposed to broad diffuse structures. Based on the previous works of Bouvier *et al.* and Abel *et al.* [93–95] on the $^3A_2(0, 0, 0) - X(0, 0, 0)$ rovibronic band of $^{16}\text{O}_3$ near 10080 cm^{-1} and on previous observations of similar broad structures assigned to the $^3A_2(0, 0, 0) - X(1, 1, 0)$ hot band of the heavy $^{18}\text{O}_3$ isotopologue near the 7880 cm^{-1} band [79,80], these diffuse absorption patterns are believed to be due to rovibronic transitions reaching the metastable levels of the 3A_2 electronic triplet state from the (0,2,0) ground electronic bending state at 1399 cm^{-1} [the center of the $^3A_2(0, 0, 0) - X(0, 2, 0)$ hot band is predicted near 8154 cm^{-1}].

In addition to these rovibronic structures (two narrow ones are marked on Fig. 8), the very weak lines of the $6\nu_1 + \nu_2 + \nu_3$ band are superimposed to strong lines of impurities (in particular water and CO_2) and other weaker narrow lines which are believed to belong to ozone but remain to be identified. To make the comparison clearer, we have extracted in the middle panel of Fig. 7 the lines of the $6\nu_1 + \nu_2 + \nu_3$ band for which line parameters were derived from a fit of their line profile. Care has to be taken for interpretation of fine details in such a comparison because of the presence of overlapping multiplets,

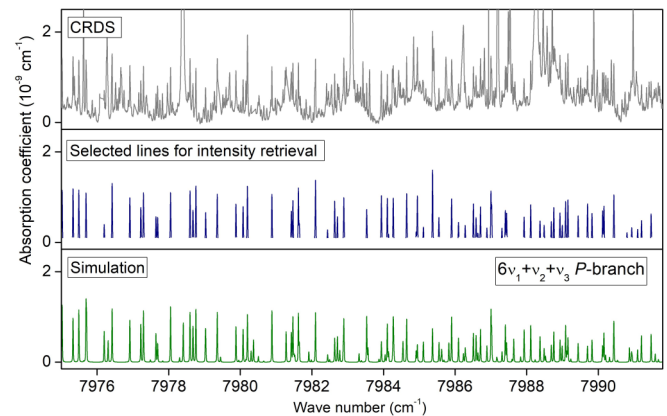


FIG. 7. Spectrum overview in the region of P branch of the $6\nu_1 + \nu_2 + \nu_3$ band of $^{16}\text{O}_3$. Upper panel: CRDS spectrum including the $6\nu_1 + \nu_2 + \nu_3$ band, impurity lines (water and CO_2), broad structures due to the $^3A_2(0, 0, 0) - X(0, 2, 0)$ vibronic hot band of $^{16}\text{O}_3$ and additional unidentified lines of ozone. Middle panel: lines of the $6\nu_1 + \nu_2 + \nu_3$ band of $^{16}\text{O}_3$ which were reproduced with a Voigt profile fit. The plotted lines are simulations based on the retrieved line profile parameters. Lower panel: simulation limited to transitions reaching experimentally determined upper levels with intensities computed from EH and EDM parameters (Table II) and line positions empirically corrected.

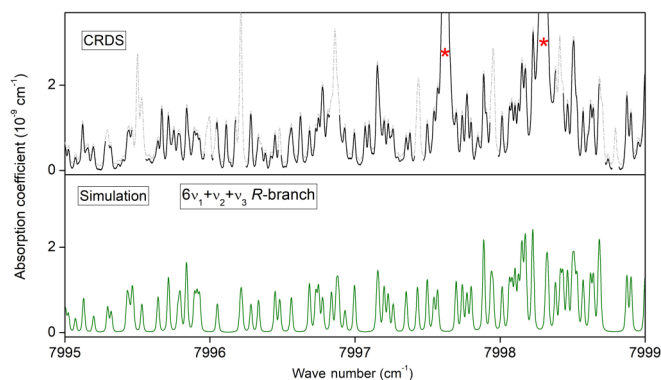


FIG. 8. Same as Fig. 9 in the region R branch of the $6\nu_1 + \nu_2 + \nu_3$ band of $^{16}\text{O}_3$. The original spectrum including impurity lines is also displayed on the upper panel (dashed grey). Relatively broad features marked with asterisks correspond to electronic $^3A_2(0, 0, 0) - X^1A_1(0, 2, 0)$ hot band transitions.

some of them not belonging to the assigned band. However, the general agreement of the intensity patterns in the measured (middle panel) and calculated (lower panel) spectra validates the assignments of the $6\nu_1 + \nu_2 + \nu_3$ band.

IV. DISCUSSION AND CONCLUSIONS

The role of the vibration-rotational states near the dissociation threshold is a long-standing concern in molecular dynamics [11]. In the “status review report” for the ozone studies, Schinke *et al.* [10] noted that experimental kinetic “rate coefficients are highly averaged quantities... that renders it difficult to assess the applicability and accuracy of any theoretical approach. More detailed ... spectroscopic data slightly below and above the threshold would be instrumental in checking the shape of the PES in the transition states region and verifying quantum-mechanical resonance calculations. We are aware that such experiments pose a real challenge.” At that time high-resolution spectroscopy measurements were only able to access rovibrational states up to 80% of D_0 [63].

Guillon *et al.* [25] have recently shown that inaccurate theoretical modeling of isotopic oxygen exchange reactions $^n\text{O}_2 + ^m\text{O} \Rightarrow ^n\text{O} + ^m\text{O}$ (with $m, n = 16$ or 18) results from a lack of understanding of rovibrationally metastable ozone O_3^* properties at energies near the dissociation threshold. An agreement with experiments for their qualitative and quantitative behaviors in the first-principle dynamical calculations [25,26] could only be obtained from a spectroscopically accurate ozone PES.

The problem with the spectroscopic validation is that intensities of rovibrational bands in the ranges approaching the dissociation threshold fall down very rapidly as is illustrated in the log-scale scheme of Fig. 9, where all previous measurements are compiled together with the results of the present work.

Previous CRDS measurements of our group [62,73] permitted us to probe the transition-state (TS) ranges of the PES between the molecular equilibrium and dissociation fragments, which have a crucial importance for the above-mentioned processes [10,24–27,38]. This has clearly shown

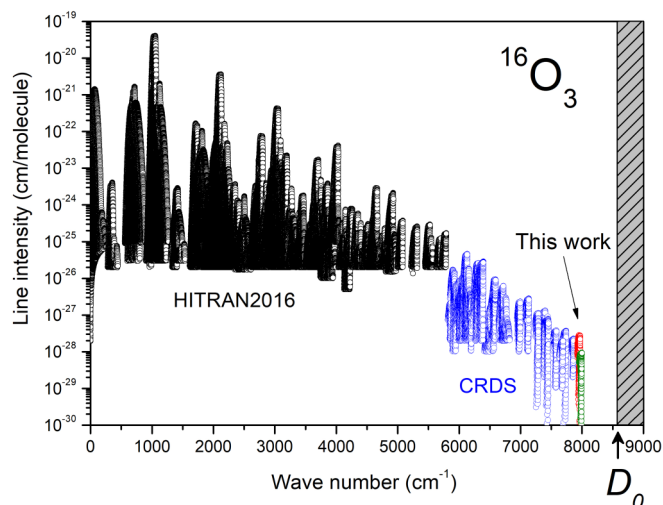


FIG. 9. Overview of the line lists of the analyzed rovibrational bands of $^{16}\text{O}_3$. Up to 5850 cm^{-1} , the line list provided by the HITRAN2016 database [60] (black circles) is reproduced. The CRDS data of Refs. [64–74] cover the $5850\text{--}7900\text{ cm}^{-1}$ region (blue circles) while the most excited bands above 7900 cm^{-1} are the $\nu_1 + 6\nu_2 + 3\nu_3$ band (red) and $6\nu_1 + \nu_2 + \nu_3$ (green) bands studied in this work. The dissociation threshold (8560 cm^{-1} [16]) is indicated.

that many published PESs ([10,35,36,96] and references therein) exhibiting an activation barrier or a so-called “reef structure” [97] (with a submerged barrier on the minimum-energy path below the dissociation limit) are not consistent with high-resolution spectroscopy observations.

The present work not only confirms these results, but extends observations beyond this range. The exceptional sensitivity of the CRDS experimental setup used in the present work has allowed for the detection and analysis of two extremely weak combination bands of $^{16}\text{O}_3$ above 7900 cm^{-1} , with upper states involving up to ten vibrational quanta (Figs. 4–8). The two reported bands are the highest energy bands reported so far. Their intensity is smaller by nine orders of magnitude (Fig. 9) compared to the fundamental bands [54,98]. The assignment of 432 transitions of the $\nu_1 + 6\nu_2 + 3\nu_3$ and $6\nu_1 + \nu_2 + \nu_3$ bands allowed us to determine 240 upper state vibration-rotation levels between 7969 and 8277 cm^{-1} (see Fig. 10). This represents the highest so far obtained experimental set of rotationally resolved data up to $J_{\text{max}} = 25$ in the 93.1–96.7% range of the dissociation threshold (where the highest energy level is $(J, K_a, K_c) = (3, 22, 25)$ having the energy of 8277.3 cm^{-1}).

Comparisons with *ab initio* calculations and analyses of rotational patterns (Sec. III) are of key importance for understanding vibrational dynamics. The most widely used PESs are full-dimensional *ab initio* ozone surfaces of Seibert *et al.* (SSB PES) [35], Tyuterev *et al.* (TKTHS NR_PES) [15], and Dawes *et al.* (DLLJG PES) [39]. The first one [35] has a barrier on the minimum-energy path and underestimates the dissociation limit, so that our observed cold bands would fall in the dissociation continuum of the SSB PES [35,36]. Our observations provide the experimental evidence that this is not the case, because we unambiguously assigned transitions to the bound rovibrational states within the electronic ground

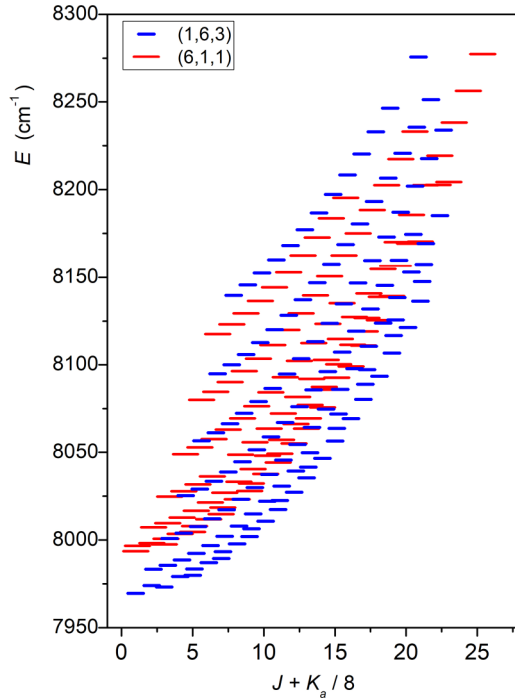


FIG. 10. Experimentally determined vibration-rotation levels of the (1,6,3) and (6,1,1) vibrational states of $^{16}\text{O}_3$ as a function of the rotational quantum numbers J and K_a (short blue and long red symbols, respectively).

state having characteristic thin line profile shapes (Figs. 4–8). The other two surfaces [15,39] have very accurate threshold D_0 values with an error estimation of about $\pm 0.5\%$ and exhibit a kind of “smooth shoulders” [38] instead of the “reef” barrier [97] at the transition state range with somewhat different shapes as summarized in Fig. 1 of Ref. [25]. A comparison of key features of these PESs including fundamental frequencies and dissociation energy can be found in Table I by Yuen *et al.* [27]. Compared to our band observed near 7993 cm^{-1} , the nearest parallel band center calculated [40,41] from the DLLJG PES [39] is about 9 cm^{-1} off, whereas for the band at 7969 cm^{-1} , the nearest calculated parallel band center [41]

is about 27 cm^{-1} off. This is similar to the dispersion of the (obs.-calc.) values displayed in Fig. 9 of Ref. [18] and comparable with the average separation between vibrational levels. Moreover, for the latter band analyzed in Sec. III C, the upper state vibrational assignment (1,9,1) of [41] is not consistent with experimentally determined rotational constants of the observed (1,6,3) state.

For the band center values computed [15,17,18] from the *ab initio* TKTHS PES [15], the (obs.-calc.) errors are by an order of magnitude smaller, about 1 and 2.5 cm^{-1} , correspondingly. In addition, the vibrational dependence of rotational constants provides valuable information for comparison with *ab initio* calculations and for reliable spectra analyses. Predicted values of A_V , B_V , C_V were critical for the rovibrational assignments, as they essentially determine the distance between the band centers and the bandheads. The overall agreement (Table IV) is almost as good as for bands at lower energy [52,62,73,74] confirming the accuracy of the *ab initio* “nonreef” TKTHS PES [15] in this very high-energy range.

In the context of the nuclear dynamics, an important question concerns possible experimental manifestations of the interactions among the three identical C_{2V} potential wells [17,18,22,35,36,49] of the ozone molecule corresponding to the lowest “open” geometrical configurations, which appear to be due to Jahn-Teller effect. The theoretical background including conical intersections of electronic states responsible for this effect in case of ozone has been described by Tannor [49], Garcia-Fernandez *et al.* [19], and Alijah *et al.* [22]. In this context, it is instructive to examine in more detail the comparison for the band centers E_V with *ab initio* predictions using two types of recent variational calculations in a single well and in three potential wells. It is well-known that the equilibrium geometry of ozone molecule corresponds to $(r^{(e)}_{13} = 4.1a_0) > (r^{(e)}_{12} = r^{(e)}_{23} = 2.4a_0)$, where low case indices stand for $\text{O}_{(1)}$ and $\text{O}_{(3)}$ edge oxygen atoms and $\text{O}_{(2)}$ for the central oxygen atom making ozone an asymmetric top molecule of C_{2V} point group. The first variational method [15] was constrained to bound levels calculations within one potential well of the “open-state” configuration belonging to the C_{2V} point group, which corresponds to the geometrical

TABLE IV. Comparison of experimentally determined band centers and upper state rotational constants with predictions from *ab initio* PES [15] using two methods of variational calculations.

Upper state		Expt. (TW)	One-well (C_{2V}) [15]		Three-wells [$D_{3h}(M)$] [17,18]	
			<i>ab initio</i>	Expt.-Calc.	<i>ab initio</i>	Expt.-Calc.
(1,6,3)	E_V	7968.78	7971.69	-2.91	7971.12	-2.34
	A_V	3.448	3.472	-0.023	3.442	0.006
	B_V	0.402	0.396	0.006	0.388	0.014
	C_V	0.341	0.348	-0.007	0.344	-0.003
(6,1,1)	E_V	7992.83	7991.66	1.17	7991.66	1.17
	A_V	3.414	3.407	0.006	3.411	0.003
	B_V	0.417	0.416	0.002	0.410	0.007
	C_V	0.369	0.366	0.002	0.363	0.006

Notes: All values are given in cm^{-1} . TW = This work. One-well (C_{2V}): variational calculations in one potential well of C_{2V} point group. Three-wells [$D_{3h}(M)$]: variational calculations in three potential wells of $D_{3h}(M)$ symmetry group. In both variational predictions the same *ab initio* “nonreef” TKTHS PES of [15] has been used.

sector ($r_{12} < r_{13} > r_{23}$). The other variational method [17,18] is based on a full account of the permutation symmetry among three identical oxygen nuclei, corresponding to the $D_{3h}(M)$ group using symmetry adapted hyperspherical coordinates [99–101]. *Ab initio* TKTHS PES [15] was the same in both calculations with the same shape in the transition state range and towards the dissociation limit, just symmetrized in three sectors of nuclear geometries ($r_{12} < r_{13} > r_{23}$; $r_{13} < r_{12} > r_{23}$; and $r_{12} < r_{23} > r_{13}$). This gives rise to three identical potential wells separated by barriers. Three different arrangements of the oxygen atoms are thus placed in these three potential wells [17,18,19,22,35,49].

For all centers of parallel bands of ozone experimentally measured up to now [52,53,64–73], both theoretical approaches produced identical values (with differences $\sim 0.01 \text{ cm}^{-1}$ or less) [15,17]. According to a very recent theoretical study by Kokouline *et al.* [18], the first notable difference of 0.57 cm^{-1} is predicted for the ($B_1, 89$) vibration level in the C_{2v} point-group notations. In the present work, we were able to observe the rovibrational transitions corresponding to this particular level that we assigned to the (1,6,3) vibration, according to the dominant normal-mode contribution on the potential surface [15] supporting the nuclear motion. It is expected that the discrepancies between the one-well and three-wells calculations should increase towards the D_0 threshold. Theoretically this is explained by interactions among the three potential wells [18] that had not been experimentally evidenced up to now. Though at this stage of the study it is too early to claim for an experimental proof of such coupling effects, the comparison (Table IV) with our experimental value for the level (1,6,3) gives a hint that the three-wells predictions go to the right direction slightly diminishing the *ab initio* error by more than 20%.

The role of various vibrational states for the molecular dynamics near the dissociation threshold is expected to be quite different depending on the type of nuclear motion. Highly excited vibrations with large symmetric stretch quantum number ν_1 [as the (6,1,1) state near 7993 cm^{-1} analyzed in Sec. III C] might be a precursor for the series of metastable states [102] having relatively long lifetimes, as theoretically studied by Lapierre *et al.* [17]. They are essentially localized in one potential well [18]. On the contrary, the vibrational states where ν_3 and ν_2 are simultaneously excited [as is the case of the (1,6,3) state near 7969 cm^{-1} analyzed in Sec. III B] could be precursors of the “roaming” series [103,104] pointing towards another potential well [18]. These series will contribute in the processes of nuclear permutation, which are particularly important in the case of isotopic exchange reactions [10,23–27]. We have observed (Sec. III) that for the $\nu_1 + 6\nu_2 + 3\nu_3$ band, the effect of J, K_a -specific behavior of the rotational series was much more pronounced than for the $6\nu_1 + \nu_2 + \nu_3$ band. This provides additional experimental insight confirming the theoretical findings of the different impact of the interaction between the three wells depending on the forms of vibrational motion [18]. A particular sensitivity of the (1,6,3) state to this interaction is supported by vibrational dynamics considerations: a simultaneous excitation of the high bending ($\nu_2 = 6$) and asymmetric stretching ($\nu_3 = 3$) modes points in the direction towards another potential well

[18] making the molecule more floppy. Such effect is not expected in the (6,1,1) state where quite rigid symmetric stretch vibrations ($\nu_1 = 6$) are activated (the one-well and three-wells *ab initio* values are identical for this latter state - see Table IV).

Another issue attracting considerable interest, both for fundamental molecular physics [43–45] and for non-LTE applications [32–34,42], concerns the dependence of the transition probabilities (and related radiative Einstein coefficients) *versus* vibrational excitations at high energy. Our past [64–73] and present CRDS measurements show, quite surprisingly, a relative importance of the combination bands involving a large variation of bending quantum number ν_2 , like the $\nu_1 + 6\nu_2 + 3\nu_3$ band which is three times stronger than the $6\nu_1 + \nu_2 + \nu_3$ band dominated by stretching normal-mode contribution (Tables II and III and Figs. 4–8). This was not expected from the measurements in lower wave number ranges where the band intensities nearly vanish with increasing ν_2 values: the $2\nu_2$ band is relatively weak, whereas the bending overtone bands $3\nu_2, 4\nu_2, 5\nu_2, \dots$ have never been observed, except for a few lines borrowing their intensities *via* accidental resonances from the stretching bands as reviewed in [52,53,82]. Note that non-LTE radiative transfer models employed for interpretation of satellite ozone measurement [32–34,42] rely on Einstein coefficients for rovibrational bands (Table G.1 of [33]), generally obtained *via* extrapolations based on simple harmonic oscillator wave functions. For the high-energy vibrations, such extrapolations could result in errors by several orders of magnitude because of the complicated shape of the PES and of the dipole moment surface [82]. More advanced calculations and measurements are necessary to obtain a global reliable picture of related radiative processes, at least at the qualitative level. The Einstein coefficients for the transitions of our two assigned bands involving large changes in vibrational quantum numbers could contribute to a better understanding and modeling of the ozone dynamics including non-LTE processes.

The effects of the interactions among the three potential wells should be confirmed by further observations above 8000 cm^{-1} . Besides the experimental challenge, an extension of the analyses towards D_0 will require accurate theoretical predictions both for hot bands in electronic transitions $^3A_2(0, 0, 0) \rightarrow X(\nu_1, \nu_2, \nu_3)$ and *ab initio* intensities of rovibrational bands with large variation of vibration quantum numbers, which up to now were limited by $\Delta\nu_{\text{max}} = 6$ [82]. A study of qualitative changes of vibrational modes [105] on global *ab initio* PESs will be helpful for band assignments as well as for the account of deviations from the Born-Oppenheimer approximation [106] and of nonadiabatic interactions of electronic states [19–22] near the dissociation asymptote.

ACKNOWLEDGMENTS

Support from the Russian Science Foundation (Project No. RNF-19-12-00171) and CNRS (France) in the frame of the International Research Project SAMIA with IAO Tomsk are acknowledged. We are grateful to S. Tashkun (IAO, Tomsk, Russia) for collaboration in software development.

- [1] P. Fabian and M. Dameris, *Ozone in the Atmosphere: Basic Principles, Natural and Human Impacts* (Springer Science & Business, Berlin, Heidelberg, 2014).
- [2] R. Müller, *Phys. Rev. Lett.* **91**, 058502 (2003).
- [3] Q.-B. Lu, *Phys. Rev. Lett.* **102**, 118501 (2009).
- [4] L. Hu, D. J. Jacob, X. Liu, Y. Zhang, L. Zhang, P. S. Kim, M. P. Sulprizio, and R. M. Yantosca, *Atmos. Env.* **167**, 323 (2017).
- [5] Y. Q. Gao and R. A. Marcus, *Science* **293**, 259 (2001).
- [6] C. Janssen and R. Marcus, *Science* **294**, 951 (2001).
- [7] D. Charlo and D. C. Clary, *J. Chem. Phys.* **120**, 2700 (2004).
- [8] K. Luther, K. Oum, and J. Troe, *Phys. Chem. Chem. Phys.* **7**, 2764 (2005).
- [9] T. Xie and J. M. Bowman, *Chem. Phys. Lett.* **412**, 131 (2005).
- [10] R. Schinke, S. Y. Grebenshchikov, M. Ivanov, and P. Fleurat-Lessard, *Annu. Rev. Phys. Chem.* **57**, 625 (2006).
- [11] R. A. Marcus, *Proc. Natl. Acad. Sci. USA* **110**, 17703 (2013).
- [12] T. R. Rao, G. Guillon, S. Mahapatra, and P. Honvault, *J. Phys. Chem. Lett.* **6**, 633 (2015).
- [13] A. Teplukhin and D. Babikov, *Phys. Chem. Chem. Phys.* **18**, 19194 (2016).
- [14] F. Holka, P. G. Szalay, T. Muller, and V. G. Tyuterev, *J. Phys. Chem. A* **114**, 9927 (2010).
- [15] V. G. Tyuterev, R. V. Kochanov, S. A. Tashkun, F. Holka, and P. G. Szalay, *J. Chem. Phys.* **139**, 134307 (2013).
- [16] B. Ruscic, unpublished results obtained from active thermochemical tables (ATcT) based on the Core (Argonne), Thermochemical Network version 1.110, 2010. Available at atct.anl.gov.
- [17] D. Lapierre, A. Alijah, R. Kochanov, V. Kokoouline, and V. Tyuterev, *Phys. Rev. A* **94**, 042514 (2016).
- [18] V. Kokoouline, D. Lapierre, A. Alijah, and V. Tyuterev, *Phys. Chem. Chem. Phys.* **22**, 15885 (2020).
- [19] P. Garcia-Fernandez, I. B. Bersuker, and J. E. Boggs, *Phys. Rev. Lett.* **96**, 163005 (2006).
- [20] P. Rosmus, P. Palmieri, and R. Schinke, *J. Chem. Phys.* **117**, 4871 (2002).
- [21] M. Tashiro and R. Schinke, *J. Chem. Phys.* **119**, 10186 (2003).
- [22] A. Alijah, D. Lapierre, and V. Tyuterev, *Mol. Phys.* **116**, 2660 (2018).
- [23] P. Fleurat-Lessard, S. Y. Grebenshchikov, R. Schinke, C. Janssen, and D. Krankowsky, *J. Chem. Phys.* **119**, 4700 (2003).
- [24] Z. Sun, D. Yu, W. Xie, J. Hou, R. Dawes, and H. J. Guo, *J. Chem. Phys.* **142**, 174312 (2015).
- [25] G. Guillon, P. Honvault, R. Kochanov, and V. Tyuterev, *J. Phys. Chem. Lett.* **9**, 1931 (2018).
- [26] P. Honvault, G. Guillon, R. Kochanov, and V. Tyuterev, *J. Chem. Phys.* **149**, 214304 (2018).
- [27] C. H. Yuen, D. Lapierre, F. Gatti, V. Kokoouline, and V. G. Tyuterev, *J. Phys. Chem. A* **123**, 7733 (2019).
- [28] M. H. Thiemens and J. E. Heidenreich, *Science* **219**, 1073 (1983).
- [29] D. Krankowsky and K. Mauersberger, *Science* **274**, 1324 (1996).
- [30] M. Kaufmann, S. Gil-López, M. López-Puertas, B. Funke, M. García-Comas, N. Glatthor, U. Grabowski, M. Höpfner, G. P. Stiller, T. von Clarmann, M. E. Koukoulis, L. Hoffmann, and M. Riese, *J. Atmos. Sol. Terr. Phys.* **68**, 202 (2006).
- [31] J. M. Flaud and J. Orphal, in *Handbook of High-Resolution Spectroscopy*, edited by M. Quack and F. Merkt (John Wiley & Sons, London, 2011), p. 1971.
- [32] A. K. Smith, V. L. Harvey, M. G. Mlynczak, B. Funke, M. García-Comas, M. Hervig, M. Kaufmann, E. Kyrölä, M. López-Puertas, I. McDade, C. E. Randall, J. M. Russell III, P. E. Sheese, M. Shiotani, W. R. Skinner, M. Suzuki, and K. A. Walker, *J. Geophys. Res. Atmos.* **118**, 5803 (2013).
- [33] M. Lopez-Puertas and F. W. Taylor, *NON-LTE Radiative Transfer in the Atmosphere. Series on Atmospheric, Oceanic and Planetary Physics* (World Scientific, Singapore, 2001), Vol. 3.
- [34] A. G. Feofilov and A. A. Kutepov, *Surv. Geophys.* **33**, 1231 (2012).
- [35] R. Siebert, R. Schinke, and M. Bittererova, *Phys. Chem. Chem. Phys.* **3**, 1795 (2001).
- [36] R. Siebert, P. Fleurat-Lessard, R. Schinke, M. Bittererova, and S. Farantos, *J. Chem. Phys.* **116**, 9749 (2002).
- [37] S. Y. Grebenshchikov, Z.-W. Qu, H. Zhu, and R. Schinke, *Phys. Chem. Chem. Phys.* **9**, 2044 (2007).
- [38] R. Dawes, P. Lolur, J. Ma, and H. Guo, *J. Chem. Phys.* **135**, 081102 (2011).
- [39] R. Dawes, P. Lolur, A. Li, B. Jiang, and H. Guo, *J. Chem. Phys.* **139**, 201103 (2013).
- [40] S. Ndengué, R. Dawes, X.-G. Wang, T. Jr. Carrington, Z. Sun, and H. Guo, *J. Chem. Phys.* **144**, 074302 (2016).
- [41] A. Teplukhin and D. Babikov, *J. Chem. Phys.* **145**, 114106 (2016).
- [42] B. Funke, M. Lopez-Puertas, M. Garcia-Comas, M. Kaufmann, M. Hopfner, and G. P. Stiller, *J. Quant. Spectrosc. Radiat. Transf.* **113**, 1771 (2012).
- [43] E. Medvedev, V. Ushakov, E. Conway, A. Upadhyay, I. Gordon, and J. Tennyson, *J. Quant. Spectrosc. Radiat. Transfer* **252**, 107084 (2020).
- [44] E. S. Medvedev, *J. Chem. Phys.* **137**, 174307 (2012).
- [45] K. K. Lehmann and A. M. Smith, *J. Chem. Phys.* **93**, 6140 (1990).
- [46] A. L. Van Wyngarden, K. A. Mar, K. A. Boering, J. J. Lin, Y. T. Lee, S.-Y. Lin, H. Guo, and G. Lendvay, *J. Am. Chem. Soc.* **129**, 2866 (2007).
- [47] Z. Sun, L. Liu, S. Y. Lin, R. Schinke, H. Guo, and D. H. Zhang, *Proc. Natl. Acad. Sci. USA* **107**, 555 (2010).
- [48] A. L. Van Wyngarden, K. A. Mar, J. Quach, A. P. Q. Nguyen, A. A. Wiegel, S.-Y. Lin, G. Lendvay, H. Guo, J. J. Lin, Y. T. Lee, and K. A. Boering, *J. Chem. Phys.* **141**, 064311 (2014).
- [49] D. J. Tannor, *J. Am. Chem. Soc.* **111**, 2772 (1989).
- [50] J. M. Flaud, C. Camy-Peyret, C. P. Rinsland, M. A. Smith, and V. Malathy Devi, *Atlas of Ozone Spectral Parameters from Microwave to Medium Infrared* (Academic, Boston, 1990).
- [51] J. M. Flaud and R. Bacis, *Spectrochim. Acta, Part A* **54**, 3 (1998).
- [52] A. Barbe, S. Mikhailenko, E. Starikova, M.-R. De Backer, V. G. Tyuterev, D. Mondelain, S. Kassi, A. Campargue, C. Janssen, S. Tashkun, R. Kochanov, R. Gamache, and J. Orphal, *J. Quant. Spectrosc. Radiat. Transfer* **130**, 172 (2013).
- [53] Y. L. Babikov, S. N. Mikhailenko, A. Barbe, and V. G. Tyuterev, *J. Quant. Spectrosc. Radiat. Transfer* **145**, 169 (2014).

- [54] G. Wagner, M. Birk, F. Schreir, and J. M. Flaud, *J. Geophys. Res.* **107**, 4626 (2002).
- [55] A. Barbe, E. Starikova, M.-R. De Backer, and Vl. G. Tyuterev, *J. Quant. Spectrosc. Radiat. Transfer* **218**, 231 (2018).
- [56] S. Mikhailenko and A. Barbe, *J. Quant. Spectrosc. Radiat. Transfer* **244**, 106823 (2020).
- [57] J. Hodges, J. Viallon, P. Brewer, B. Drouin, V. Gorschelev, C. Janssen, S. Lee, A. Possolo, M. A. H. Smith, J. Walden, and R. I. Wielgosz, *Metrologia* **56**, 034001 (2019).
- [58] E. Starikova, A. Barbe, and V. Tyuterev, *J. Quant. Spectrosc. Radiat. Transfer* **232**, 87 (2019).
- [59] M. Birk, G. Wagner, I. E. Gordon, and B. J. Drouin, *J. Quant. Spectrosc. Radiat. Transfer* **226**, 60 (2019).
- [60] I. E. Gordon, L. S. Rothman, C. Hill, R. V. Kochanov, Y. Tan, P. F. Bernath *et al.*, *J. Quant. Spectrosc. Radiat. Transfer* **203**, 3 (2017).
- [61] N. Jacquinet-Husson, R. Armante, N. A. Scott, A. Chédin, L. Crépeau, C. Boutammine *et al.*, *J. Mol. Spectrosc.* **327**, 31 (2016).
- [62] V. G. Tyuterev, R. Kochanov, A. Campargue, S. Kassı, D. Mondelain, A. Barbe, E. Starikova, M. R. De Backer, P. G. Szalay, and S. Tashkun, *Phys. Rev. Lett.* **113**, 143002 (2014).
- [63] H. Wenz, W. Demtröder, and J. M. Flaud, *J. Mol. Spectrosc.* **209**, 267 (2001).
- [64] A. Campargue, D. Romanini, S. Kassı, A. Barbe, M.-R. De Backer-Barilly, and Vl. G. Tyuterev, *J. Mol. Spectrosc.* **240**, 1 (2006).
- [65] M.-R. De Backer-Barilly, A. Barbe, Vl. G. Tyuterev, D. Romanini, B. Moeskops, and A. Campargue, *J. Mol. Struct.* **780-781**, 225 (2006).
- [66] A. Barbe, M.-R. De Backer-Barilly, Vl. G. Tyuterev, A. Campargue, D. Romanini, and S. Kassı, *J. Mol. Spectrosc.* **242**, 156 (2007).
- [67] S. Kassı, A. Campargue, M.-R. De Backer-Barilly, and A. Barbe, *J. Mol. Spectrosc.* **244**, 122 (2007).
- [68] A. Barbe, M.-R. De Backer-Barilly, Vl. G. Tyuterev, S. Kassı, and A. Campargue, *J. Mol. Spectrosc.* **246**, 22 (2007).
- [69] A. Campargue, A. Barbe, M.-R. De Backer-Barilly, Vl. G. Tyuterev, and S. Kassı, *Phys. Chem. Chem. Phys.* **10**, 2925 (2008).
- [70] D. Mondelain, A. Campargue, S. Kassı, A. Barbe, E. Starikova, M. R. De Backer, and Vl. G. Tyuterev, *J. Quant. Spectrosc. Radiat. Transfer* **116**, 49 (2013).
- [71] A. Barbe, M.-R. De Backer-Barilly, Vl. G. Tyuterev, S. Kassı, and A. Campargue, *J. Mol. Spectrosc.* **269**, 175 (2011).
- [72] M.-R. De Backer-Barilly, A. Barbe, E. Starikova, Vl. G. Tyuterev, S. Kassı, and A. Campargue, *J. Mol. Spectrosc.* **272**, 43 (2012).
- [73] A. Campargue, S. Kassı, D. Mondelain, A. Barbe, E. Starikova, M.-R. De Backer-Barilly, and Vl. G. Tyuterev, *J. Quant. Spectrosc. Radiat. Transfer* **152**, 84 (2015).
- [74] E. Starikova, D. Mondelain, A. Barbe, Vl. G. Tyuterev, S. Kassı, and A. Campargue, *J. Quant. Spectrosc. Radiat. Transfer* **161**, 203 (2015).
- [75] M. Konefat, D. Mondelain, S. Kassı, and A. Campargue, *J. Quant. Spectrosc. Radiat. Transfer* **241**, 106653 (2020).
- [76] E. V. Karlovets, S. Kassı, and A. Campargue, *J. Quant. Spectrosc. Radiat. Transfer* **247**, 106942 (2020).
- [77] M. Griggs, *J. Chem. Phys.* **49**, 857 (1968).
- [78] S. Suzuki, I. M. Rusinov, K. Teranishi, N. Shimomura, and H. Ito, *J. Phys. D: Appl. Phys.* **51**, 305201 (2018).
- [79] D. Mondelain, S. Kassı, R. Jost, and A. Campargue, *Chem. Phys. Lett.* **510**, 191 (2011).
- [80] D. Mondelain, R. Jost, S. Kassı, R. H. Judge, Vl. G. Tyuterev, and A. Campargue, *J. Quant. Spectrosc. Radiat. Transfer* **113**, 840 (2012).
- [81] A. Barbe, A. Chichery, T. Cours, Vl. G. Tyuterev, and J. J. Plateaux, *J. Mol. Struct.* **616**, 55 (2002).
- [82] V. G. Tyuterev, R. V. Kochanov, and S. A. Tashkun, *J. Chem. Phys.* **146**, 064304 (2017).
- [83] S. A. Tashkun and Vl. G. Tyuterev, *SPIE Proc.* **2205**, 188 (1994).
- [84] J. J. Plateaux, L. Régalia, C. Boussin, and A. Barbe, *J. Quant. Spectrosc. Radiat. Transfer* **68**, 507 (2001).
- [85] Vl. G. Tyuterev, S. A. Tashkun, and H. Seghir, *SPIE Proc.* **5311**, 164 (2004).
- [86] V. Tyuterev, S. A. Tashkun, M. Rey, R. Kochanov, A. Nikitin, and T. Delahaye, *J. Phys. Chem. A* **117**, 13779 (2013).
- [87] A. Barbe, S. Bouazza, J. J. Plateaux, and M. Jacon, *J. Mol. Spectrosc.* **162**, 335 (1993).
- [88] J. K. G. Watson, *J. Chem. Phys.* **46**, 1935 (1967).
- [89] J.-M. Flaud, C. Camy-Peyret, V. Malathy Devi, C. P. Rinsland, and M. A. H. Smith, *J. Mol. Spectrosc.* **124**, 209 (1987).
- [90] C. Camy-Peyret and J.-M. Flaud, Ph.D. thesis, Paris, 1975.
- [91] O. N. Sulakshina, Yu. Borkov, Vl. G. Tyuterev, and A. Barbe, *J. Chem. Phys.* **113**, 10572 (2000).
- [92] See Supplemental Material at <http://link.aps.org/supplemental/10.1103/PhysRevA.102.052804> for the results of the fit of the effective dipole transition moment to the measured intensities of the $\nu_1 + 6\nu_2 + 3\nu_3$ band of $^{16}\text{O}_3$, results of the fit of the effective dipole transition moment to the measured intensities of the $6\nu_1 + \nu_2 + \nu_3$ band of $^{16}\text{O}_3$, diagrams of measured and calculated intensities of the $\nu_1 + 6\nu_2 + 3\nu_3$ and $6\nu_1 + \nu_2 + \nu_3$ bands of $^{16}\text{O}_3$, and calculated line lists of the $\nu_1 + 6\nu_2 + 3\nu_3$ and $6\nu_1 + \nu_2 + \nu_3$ bands of $^{16}\text{O}_3$.
- [93] A. J. Bouvier, G. Wannous, S. Churassy, R. Bacis, J. Brion, J. Malicet, and R. H. Judge, *Spectro. Acta* **57**, 561 (2001).
- [94] B. Abel, A. Charvat, and S. Deppe, *Chem. Phys. Lett.* **277**, 347 (1997).
- [95] U. Wachsmuth and B. Abel, *J. Geophys. Res.* **108**, 4473 (2003).
- [96] M. Ayouz and D. Babikov, *J. Chem. Phys.* **138**, 164311 (2013).
- [97] P. Fleurat-Lessard, S. Y. Grebenshchikov, R. Siebert, R. Schinke, and N. Halberstadt, *J. Chem. Phys.* **118**, 610 (2003).
- [98] Vl. G. Tyuterev, A. Barbe, D. Jacquemart, C. Janssen, S. Mikhailenko, and E. Starikova, *J. Chem. Phys.* **150**, 184303 (2019).
- [99] V. Kokoouline and C. H. Greene, *Phys. Rev. A* **68**, 012703 (2003).
- [100] V. Kokoouline and F. Masnou-Seeuws, *Phys. Rev. A* **73**, 012702 (2006).
- [101] A. Alijah, J. Fremont, and V. G. Tyuterev, *Phys. Rev. A* **92**, 012704 (2015).
- [102] B. Y. Chang, C. Y. Kung, C. Kittrell, C. W. Hsio, B. R. Johnson, S. G. Glogover, and J. L. Kinsey, *J. Chem. Phys.* **101**, 1914 (1994).

- [103] J. M. Bowman, *Mol. Phys.* **112**, 2516 (2014).
- [104] F. A. Mauguiere, P. Collins, Z. C. Kramer, B. K. Carpenter, G. S. Ezra, S. C. Farantos, and S. Wiggins, *J. Chem. Phys.* **144**, 054107 (2016).
- [105] O. V. Egorov, F. Mauguiere, and V. G. Tyuterev, *Russ. Phys. J.* **62**, 1917 (2020).
- [106] A. Tajti, P. G. Szalay, R. Kochanov, and V. G. Tyuterev, *Phys. Chem. Chem. Phys.* (2020), doi: [10.1039/D0CP02457K](https://doi.org/10.1039/D0CP02457K).